DOI: 10.1016/j.jmrt.2024.09.166

Journal of Materials Research and Technology 33 (2024) 1600–1622

Contents lists available at ScienceDirect

Journal of Materials Research and Technology

journal homepage: www.elsevier.com/locate/jmrt

Effects of Ti and Y on resistance to corrosion in Fe–Cr-X Alloys

T.J.M. Jesus [a], S.A. Souza [a], B.C. Barreto [a], A.I.C. Santana [b], R. Landers [c], R. Caram [d], M.S.C. Silva [d], J.F.Q. Rodrigues [d], C.R.M. Afonso [e], M.C.S.S. Macedo [a,*]

[a] *Department of Materials Science and Engineering (DCEM), Federal University of Sergipe (UFS), 49100-000, São Cristóvão, SE, Brazil*
[b] *Department of Metallurgy (DEPMET/FCEE), State University of Rio de Janeiro (UERJ), 23070-200, Rio de Janeiro, RJ, Brazil*
[c] *Institute of Physics Gleb Wataghin, State University of Campinas, UNICAMP, 13083-859, Campinas, SP, Brazil*
[d] *Department of Materials Engineering, Faculty of Mechanical Engineering, State University of Campinas, UNICAMP, 13083-860, Campinas, SP, Brazil*
[e] *Department of Materials Engineering (DEMa), Federal University of São Carlos (UFSCar), 13565-905, São Carlos, SP, Brazil*

ARTICLE INFO

Handling editor: SN Monteiro

Keywords:
Alloy
Stainless steel
EIS
Pitting corrosion

ABSTRACT

The effect of Ti and Y on the corrosion behavior of the FeCr alloy was investigated in a 3.5% NaCl solution. Ti was found to inhibit the formation of the σ phase, significantly reducing the presence of pitting in the material. In addition, Ti acted indirectly on the oxide layer, increasing the concentrations of Cr and Fe, consequently generating a probable enrichment of Cr_2O_3 and FeOOH, which enabled the formation of a more stable passive film resistant to attack by chloride ions. On the other hand, Y caused the precipitation of a phase identified as $Fe_{17}Y_2$, which was accompanied by an elongated σ phase, both located at the grain boundaries, besides the formation of $Cr_{23}C_6$ and Y_2O_3. Its addition resulted in an improvement in the corrosion resistance of the FeCr alloy by reducing the precipitation of the σ phase. However, its effect was much less important than that of Ti, since the results showed that the FeCrY alloy was still highly susceptible to localized forms of corrosion.

1. Introduction

The Fe–Cr system encompasses materials that have a high technological importance, such as stainless steel, whose Cr is essential for their good resistance to corrosion in several environments. The minimal concentration of 11% Cr is necessary for alloys to accomplish effective corrosion protection [1]. The oxide becomes more stable and resistant at higher concentration. However, the material is susceptible to the precipitation of secondary phases, whose type strongly depends on the other elements added to the alloy.

Studies available in the literature have assessed the influence of elements such as Mo, Si and Nb on the formation of intermetallic phases and their effects on the corrosion behavior of high-performance stainless steel [2–4]. Some of these effects have been poorly investigated, such as the case of Ti, which is often added to alloys at low concentrations. This element is easily combined to N and C, a fact that impairs the formation of compounds such as $(Fe, Cr)_x(C, N)_y$ and, consequently, avoids intergranular corrosion in the alloy [5,6]. It is known that Ti significantly affects the formation kinetics of fragile intermetallic phases, such as the sigma phase (σ), which can form a Cr content higher than 20% [7–9]. Systematic studies about the influence of Ti on resistance to pitting corrosion [10], mainly in ferrous alloys presenting high Cr contents, a condition observed in several ferritic stainless steels, remain scarce in the literature [11]. Thus, the corrosion behavior of the Fe–25Cr alloy added with 0.2% Ti was taken into consideration in the current study.

Based on such an understanding, the addition of new alloying elements was also considered with the aim of assessing the potential resistance to localized corrosion and its effects on the formation of intermetallic phases. Y stands out among alloying elements that can be added, since it is a promising element given its ability to increase resistance to corrosion by triggering significant changes in the microstructures, as observed in Al, Ni and Mg alloys [12–15]. One of the explanations suggested for these benefits lies on the fact that Y boosts the formation of new phases and improves the distribution of existing phases that enable the formation of more protective oxides on the alloy surfaces [16]. However, Y's influence on ferrous alloys is almost only seen in studies focusing on resistance to oxidation at high temperatures [13,17,18]. Therefore, the aim of the current study was to feature Fe–25Cr, Fe–25Cr-0.2Ti and Fe–25Cr-0.2Y alloys in order to assess the role of Ti and Y on microstructure and resistance to corrosion, comparing them to traditional stainless steels.

---

* Corresponding author.
E-mail address: mcardinales@academico.ufs.com (M.C.S.S. Macedo).

https://doi.org/10.1016/j.jmrt.2024.09.166
Received 10 October 2023; Received in revised form 17 September 2024; Accepted 19 September 2024

2. Materials and methods

2.1. Preparation and characterization of Fe–Cr-X alloys

The FeCr, FeCrY and FeCrTi alloys were produced as 100 g ingots by arc melting from high-purity elements (Fe (Aldrich, 99.98%), Cr (Alfa Aesar, 99.99%), Y (Aldrich, 99.9%) and Ti (Merck, 99.81%)) under an argon atmosphere (grade 5.0) in a furnace (Analogica, model AN9270) equipped with a water-cooled copper hearth and a non-consumable tungsten electrode. These alloys were melted at least eight times and flipped between each melting cycle to ensure complete melting of the elements, as well as to improve chemical homogeneity. Rolling at 980 °C was then applied to form plates with a final thickness of 2 mm, which were obtained through 6 passes. After finishing this process, the hot-rolled alloys were air-cooled to room temperature (RT), as seen in Refs. [19,20], mechanically cleaned to remove the oxide layers and cut to take samples of each composition. Impurity concentrations were measured using the Leco CS-230 for carbon, and the Leco TC-400 for nitrogen and oxygen, while the concentrations of the alloying elements of the Fe–25Cr (FeCr), Fe–25Cr-0.2Y (FeCrY) and Fe–25Cr-0.2Ti (FeCrTi) alloys and of the AISI 304 and AISI 430 stainless steels (used for comparison purposes in the electrochemical tests) were measured using a Bruker S8 TIGER WDXRF spectrometer. The chemical compositions of these materials are shown in Table 1. Regarding commercial stainless steels, their values are consistent with the ASTM A240/A240 M standard [21].

The hot-rolled samples were prepared for microstructural analysis based on standard metallographic procedures. The aqua regia solution, consisting of 75 vol% HCl and 25 vol% HNO_3, was used on the samples characterized by optical microscopy, and the 10 vol% oxalic acid solution ($H_2C_2O_4$) was applied to the samples analyzed using the scanning electron microscope (SEM, JEOL JCM - 5700). Energy dispersive X-ray spectroscopy (EDS) was used for elemental mapping and to determine the compositions of the precipitates. The X-ray diffractograms (XRD) of the samples were obtained from polished surfaces and without chemical etching using a Shimadzu LabX XRD-6000 diffractometer (40 kV, 30 mA) operated with a Cu anode (Kα radiation, $\lambda = 1.5418$ Å). Thermodynamic simulations were carried out in the temperature range from 600 to 1600 °C on FeCr, FeCrY and FeCrTi alloys using the ThermoCalc® software and the TCFE12 database. The equilibrium phases were calculated to provide a reference of the phases expected during the manufacturing process. Transmission electron microscopy (TEM) analysis was carried out using a FEI Tecnai G2 F20 200 kV (FEG) coupled to EDS together with scanning transmission electron microscopy (STEM) mode of analysis.

Table 1
Chemical compositions in wt. % of conventional stainless steels and Fe–Cr-X alloys.

Element	AISI 304	AISI 430	FeCr	FeCrY	FeCrTi
Fe	Balance	Balance	Balance	Balance	Balance
Cr	18.74 ± 0.07	16.1 ± 0.1	24.7 ± 0.1	24.71 ± 0.07	24.25 ± 0.07
Ni	8.04 ± 0.05	0.160 ± 0.001	–	–	–
Mn	1.1 ± 0.4	0.372 ± 0.006	–	–	–
Si	0.64 ± 0.06	0.30 ± 0.01	–	–	–
Y	–	–	–	0.195 ± 0.007	–
Ti	–	–	–	–	0.18 ± 0.02
C	0.0730 ± 0.0003	0.0337 ± 0.0003	0.0092 ± 0.0006	0.018 ± 0.001	0.021 ± 0.002
N	0.0470 ± 0.0001	0.0379 ± 0.0001	0.0010 ± 0.0001	0.0014 ± 0.0002	0.0003 ± 0.0001
O	0.024 ± 0.001	0.0054 ± 0.0001	0.016 ± 0.004	0.015 ± 0.001	0.0094 ± 0.0003

2.2. Electrochemical tests and characterization of the oxide layers

For electrochemical testing, each rectangular sample was embedded in polyester resin with 0.5 cm^2 of the surface area exposed and connected to the copper wire. Before the electrochemical testing, the surface of the working electrode was prepared by metallography using silicon carbide sandpapers from 200 to 1200 mesh, followed by ultrasound cleaning in ethanol and distilled water then dried in air. A three-electrode cell setup was used, which consisted of a silver/silver chloride (Ag/AgCl) saturated reference electrode, Pt counter electrode and a specimen as working electrode. All potentials in this study are given *vs* Ag/AgCl electrode. The sample was submerged in a 3.5 wt% NaCl solution without agitation and RT. Prior to all electrochemical tests, samples were immersed in the solution for 1800 s to ensure the open-circuit potential (OCP) achieved the steady state. The potentiodynamic polarization anodic curves were conducted from OCP up to + 1 V vs Ag/AgCl electrode. Chronoamperometry measurements were carried out at potentials of 0.100, 0.180 and 0.600 V, and the current was evaluated for 3600 s. These potentials were selected based on the polarization curves and correspond to the potential values where the alloys produced for this study are passivated (0.100 V), near the E_b of the FeCr and FeCrY alloys (0.180 V) and near the E_b of the FeCrTi alloy (0.600 V). Electrochemical impedance spectra (EIS) measurement was performed at a frequency ranging from 10^{-2} to 10^4 Hz with an applied 10 mV amplitude of the AC signal. Aiming to better understand the effect of Y and Ti on the corrosion behavior of the alloys, EIS test was also performed with 0.600 V versus Ag/AgCl electrode. This potential was selected for being close to the break potential (E_b) for the FeCrTi alloy. For all the electrochemical tests, the equipment used was an AUTALAB potentiostat, model PGSTAT 302 N.

After the electrochemical tests, the surfaces of the FeCr, FeCrY and FeCrTi samples were analyzed in the SEM equipment, JEOL JCM - 5700. The compositions of their passive films were also determined by X-ray Photoelectron Spectroscopy (XPS) in samples that were tested by chronoamperometry at 0.100 V for 3600 s. The XPS spectra were obtained with a VSW HA-100 spherical analyzer and AlKα radiation *($h\nu = 1486.6$ eV)*. The high-resolution spectra were measured with constant analyzer pass energy of 44 eV (which produces a full width at half-maximum (FWHM) line width of 1.6 eV for the Au ($4f_{7/2}$) line). The pressure during the measurements was always less than 6×10^{-8} mbar. The sample was fixed to a stainless-steel sample holder with double-faced conducting tape and analyzed without further preparation. Surface charging was corrected shifting all spectra so that the C1s line due to adventitious C was at 284.6 eV. Curve fitting was performed using Gaussian line shapes, and a Shirley background was subtracted from the data.

3. Results and discussion

3.1. Equilibrium phases

The volume fractions of the phases in the FeCr, FeCrY and FeCrTi alloys in the temperature range between 600 and 1600.0 °C, predicted by ThermoCalc®, are presented in Fig. 1a, b and 1c, respectively. The compositions of the phases in equilibrium at the temperatures of formation of the matrix and precipitates are also shown for the three alloys in Tables 2–4, following the same sequence as presented above. In order to obtain more suitable calculation results for microstructural analysis, the contents of impurities such as C, N and O were taken into account in the thermodynamic simulation, which are listed in Table 1. In more general terms, Fig. 1 shows that the volume fractions of the precipitated phases are very low ($<10^{-2}$) for all the alloys, as indicated in the magnified regions between 600 and 1000.0 °C, except for the σ-phase (Sigma_D8B), which reaches a value of approximately 0.14, considering

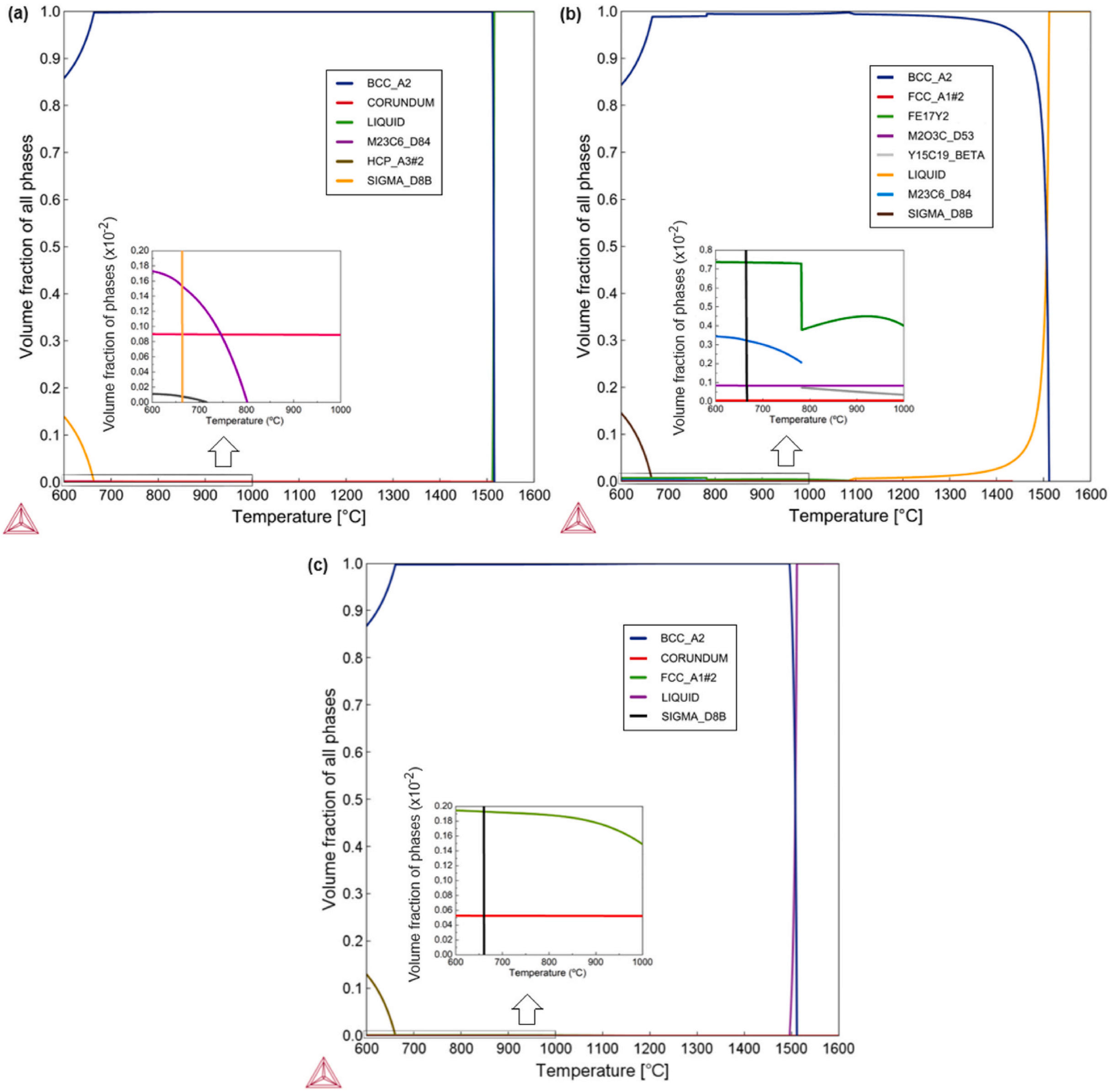

Fig. 1. Volume fraction of all phases in equilibrium between 600 and 1600 °C of FeCr (a), FeCrY (b) and FeCrTi (c) alloys predicted by ThermoCalc® software using the TCFE12 database. The interpretations of the phase conventions presented in each figure are shown in Tables 2–4, respectively. A magnified region in the range 600 to 1000 °C is also presented in each figure to better visualize the volume fractions of the minority phases.

the selected lower temperature limit. From Tables 2–4, it can be seen that its precipitation occurs at around 664 °C, being a Cr-rich phase with content close to 43 wt %, according to the simulation. Its formation causes Cr depletion in the areas adjacent to its precipitates, which makes it deleterious for corrosion resistance [3]. On the other hand, it can be seen that the oxides found in the alloys studied (Cr_2O_3, Ti_2O_3 and Y_2O_3) are beneficial to corrosive processes, but their volume fractions are quite small, not exceeding a value in the order of 10^{-3}. In the case of Y_2O_3, it should be pointed out that this oxide is unstable in aqueous media and is readily hydrated [22]. In the Pourbaix diagram of the Y–H_2O system [23], the presence of $Y(OH)_3$ can be seen, whose species is attributed with a slight protection against corrosion.

Focusing on the FeCr alloy, it can be seen that the appearance of Cr_2O_3 (corundum), at 1515.0 °C (Table 2), takes place at practically the same temperature at which α-Fe (BCC_A2) is formed, at 1515.6 °C, while $Cr_{23}C_6$ (M23C6_D84) and Cr_2N (HCP_A3#2) appear at 801.8 °C and 716.4 °C, respectively. For both $Cr_{23}C_6$ and Cr_2N, it has been well established in numerous studies that these precipitates make the alloys susceptible to intergranular corrosion [1,4]. Regarding the FeCrY alloy, it is noted that the rare earth element has brought greater complexity to the Fe–Cr system, with various types of precipitates being predicted. YN (FCC_A1#2) is formed at 1433.1 °C and remains stable, at least up to 600 °C. The combination of Y and C, on the other hand, is only maintained at high temperatures. In this case, Table 3 shows the formation of $Y_{15}C_{19}$_beta at 1095.2 °C, which occurs shortly after the precipitation of the oxide considered to be Y_2O_3 (M2O3C_D53) at 1098.7 °C. Additionally, $Fe_{17}Y_2$ precipitates at 1086.8 °C; this phase and Y_2O_3 remain stable, while $Y_{15}C_{19}$_beta disappears at 782.3 °C, concomitantly with the formation of $Cr_{23}C_6$ (M23C6_D84), not ensuring the preventive effect of Cr depletion in the α-Fe matrix. This sequence of events is also verified in the magnified region of Fig. 1b, where it can be seen that the disappearance of $Y_{15}C_{19}$_beta leads to an abrupt increase in the volume fraction of the $Fe_{17}Y_2$ phase. For the FeCrTi alloy, there is a significantly more favorable condition for corrosion resistance, with the appearance of Ti_2O_3 (corundum) in the liquid, well before the formation of α-Fe (BCC_A2), at 1511.7 °C, followed by the precipitation of Ti(C,N)

(FCC_A1#2), at 1345.1 °C.

Table 2
Compositions of the equilibrium phases in the FeCr alloy at temperatures corresponding to the formation of the phases indicated by the arrows, predicted by ThermoCalc® using the TCFE12 database.

Formation Temperature	Denomination in Fig. 1a (Phase)	Alloy Elements (wt.%)		Impurity Elements (wt.%)		
		Fe	Cr	C	N	O
	Liquid	75.3	24.7	0.009	0.001	0.02
1515.6 °C →	BCC_A2 (α-Fe)	74.8	25.2	0.002	0.0004	0.0005
	Liquid	75.4	24.6	0.01	0.001	0.02
	BCC_A2 (α-Fe)	74.9	25.1	0.002	0.0004	0.0006
1515.0 °C →	Corundum (Cr_2O_3)	0.007	68.5	0	0	31.5
	BCC_A2 (α-Fe)	75.3	24.7	0.009	0.001	1×10^{-7}
	Corundum (Cr_2O_3)	4×10^{-6}	68.7	0	0	31.3
801.8 °C →	M23C6_D84 ($Cr_{23}C_6$)	17.1	77.3	5.6	0	0
	BCC_A2 (α-Fe)	75.4	24.6	0.003	0.001	2×10^{-8}
	Corundum (Cr_2O_3)	7×10^{-7}	68.7	0	0	31.3
	M23C6_D84 ($Cr_{23}C_6$)	13.4	81.0	5.6	0	0
716.4 °C →	HCP_A3#2 (Cr_2N)	0.5	88.1	0.4	11.0	1×10^{-11}
	BCC_A2 (α-Fe)	75.4	24.6	0.001	0.0004	4×10^{-9}
	Corundum (Cr_2O_3)	2×10^{-7}	68.8	0	0	31.2
	M23C6_D84 ($Cr_{23}C_6$)	11.0	83.4	5.6	0	0
	HCP_A3#2 (Cr_2N)	0.3	88.3	0.3	11.2	1×10^{-11}
663.9 °C →	Sigma_D8B (σ)	57.3	42.7	0	0	0

3.2. Microstructural analysis

The micrographs of the FeCr, FeCrY and FeCrTi alloys are presented in Fig. 2 and show grains of different sizes with average values of 137.8 ± 61.9, 113.9 ± 61.4 and 130.9 ± 70.7 μm, respectively. The inhomogeneity in the grain sizes of these alloys, characterized by their high standard deviations, is mainly due to the behavior of the α-Fe during hot deformation. As stated in the experimental procedure, all the alloys produced were rolled at 980 °C, and their microstructures are composed of a ferritic matrix as evidenced in Fig. 1. In this case, it can be seen that the α-Fe shows continuous dynamic recrystallization during hot deformation, the behavior which is typical of materials with high stacking fault energy, where cross-slip is facilitated, and dynamic recovery becomes highly efficient. In this respect, it is important to emphasize that dynamic recovery is the dominant softening mechanism in ferritic stainless steels, which generates a low density of dislocations during high-temperature plastic deformation, and these steels may even have elongated grains [24]. This softening process is complex and not well understood, and reduces the driving force for static recrystallization. For this condition, studies indicate that static recrystallization can be stimulated using intermediate rolling temperatures, since higher temperatures stimulate recovery even more and lower temperatures do not allow recovery or recrystallization [25,26]. Other proposed solutions to improve grain homogeneity and reduce their average size are the application of annealing after changes in hot rolling practices [27] and, in this regard, it is seen that grain homogeneity can be affected by the chemical composition of the materials. Han et al. [28], for example, after hot rolling and annealing processes, observed that 18Cr–2Mo ferritic stainless steel stabilized with Nb showed a grain size distribution that was concentrated in the 60–240 μm range, whereas for the same type of steel stabilized with Nb + Ti, this range was 90–300 μm.

Table 3
Compositions of the equilibrium phases in the FeCrY alloy at temperatures corresponding to the formation of the phases indicated by the arrows, predicted by ThermoCalc® using the TCFE12 database.

Formation Temperature	Denomination in Fig. 1b (Phase)	Alloy Elements (wt.%)			Impurity Elements (wt.%)		
		Fe	Cr	Y	C	N	O
	Liquid	75.1	24.7	0.2	0.02	0.001	0.02
1512.0 °C →	BCC_A2 (α-Fe)	74.6	25.4	0.004	0.004	0.0005	9×10^{-11}
	Liquid	72.6	23.3	3.6	0.09	0.004	0.4
	BCC_A2 (α-Fe)	75.2	24.8	0.05	0.02	0.001	9×10^{-11}
1433.1 °C →	FCC_A1#2 (YN)	4×10^{-5}	0.05	86.3	6×10^{-9}	13.6	2×10^{-11}
	Liquid	58.9	18.5	19.8	0.2	8×10^{-6}	2.8
	BCC_A2 (α-Fe)	75.2	24.7	0.08	0.02	2×10^{-6}	9×10^{-11}
	FCC_A1#2 (YN)	4×10^{-8}	0.0006	86.4	2×10^{-7}	13.6	2×10^{-11}
1098.7 °C →	M2O3C_D53 (Y_2O_3)	5×10^{-11}	5×10^{-11}	78.8	0	0	21.2
	Liquid	58.8	18.2	20.1	0.2	7×10^{-6}	2.7
	BCC_A2 (α-Fe)	75.2	24.7	0.08	0.02	2×10^{-6}	9×10^{-11}
	FCC_A1#2 (YN)	3×10^{-8}	0.0005	86.4	2×10^{-7}	13.6	2×10^{-11}
	M2O3C_D53 (Y_2O_3)	5×10^{-11}	5×10^{-11}	78.8	0	0	21.2
1095.2 °C →	$Y_{15}C_{19}$_beta	0	0	85.4	14.6	0	0
	Liquid	58.7	17.5	21.0	0.2	5×10^{-6}	2.6
	BCC_A2 (α-Fe)	75.2	24.7	0.09	0.01	2×10^{-6}	9×10^{-11}
	FCC_A1#2 (YN)	3×10^{-8}	0.0004	86.3	2×10^{-7}	13.6	2×10^{-11}
	M2O3C_D53 (Y_2O_3)	5×10^{-11}	5×10^{-11}	78.8	0	0	21.8
	$Y_{15}C_{19}$_beta	0	0	85.4	14.6	0	0
1086.8 °C →	$Fe_{17}Y_2$	84.2	0	15.8	0	0	0
	BCC_A2 (α-Fe)	75.1	24.9	0.0009	0.008	2×10^{-8}	9×10^{-11}
	FCC_A1#2 (YN)	2×10^{-10}	0.0001	86.4	3×10^{-8}	13.6	2×10^{-11}
	M2O3C_D53 (Y_2O_3)	5×10^{-11}	5×10^{-11}	78.8	0	0	21.3
	$Fe_{17}Y_2$	84.2	0	15.8	0	0	0
782.3 °C →	M23C6_D84 ($Cr_{23}C_6$)	16.2	78.2	0	5.6	0	0
	BCC_A2 (α-Fe)	75.2	24.8	8×10^{-5}	0.001	1×10^{-9}	9×10^{-11}
	FCC_A1#2 (YN)	5×10^{-11}	4×10^{-5}	86.4	3×10^{-9}	13.6	2×10^{-11}
	M2O3C_D53 (Y_2O_3)	5×10^{-11}	5×10^{-11}	78.8	0	0	21.3
	$Fe_{17}Y_2$	84.2	0	15.8	0	0	0
	M23C6_D84 ($Cr_{23}C_6$)	11.1	83.3	0	5.6	0	0
666.2 °C →	Sigma_D8B (σ)	57.4	42.6	0	0	0	0

Table 4
Compositions of the equilibrium phases in the FeCrTi alloy at temperatures corresponding to the formation of the phases indicated by the arrows, predicted by ThermoCalc® using the TCFE12 database.

Formation Temperature	Denomination in Fig. 1c (Phase)	Alloy Elements (wt.%)			Impurity Elements (wt.%)		
		Fe	Cr	Ti	C	N	O
1600.0 °C*	Liquid	75.6	24.3	0.2	0.02	0.0003	0.001
	Corundum (Ti_2O_3)	0.0002	1.1	65.5	0	0	33.4
	Liquid	75.6	24.3	0.2	0.02	0.0003	0.0005
	Corundum (Ti_2O_3)	0.0001	0.8	65.9	0	0	33.4
1511.7 °C →	BCC_A2 (α-Fe)	75.1	24.8	0.06	0.005	0.0001	3×10^{-5}
1345.1 °C →	Corundum (Ti_2O_3)	5×10^{-6}	0.1	66.5	0	0	33.4
	BCC_A2 (α-Fe)	75.6	24.3	0.2	0.02	0.0003	2×10^{-6}
	FCC_A1#2 (Ti(C,N))	0.0004	0.2	79.6	7.6	12.6	0.08
	Corundum (Ti_2O_3)	2×10^{-10}	0.0002	66.6	0	0	33.4
	BCC_A2 (α-Fe)	75.7	24.3	0.06	8×10^{-6}	8×10^{-11}	9×10^{-11}
	FCC_A1#2 (Ti(C,N))	1×10^{-10}	0.02	82.3	17.5	0.2	0.002
660.8 °C →	Sigma_D8B (σ)	57.2	42.8	0.002	0	0	0

[*] Corresponds only to the temperature at which the compositions of the equilibrium phases were collected. The formation temperature of Ti_2O_3 in the FeCrTi alloy is higher than the upper temperature limit established in the thermodynamic simulation.

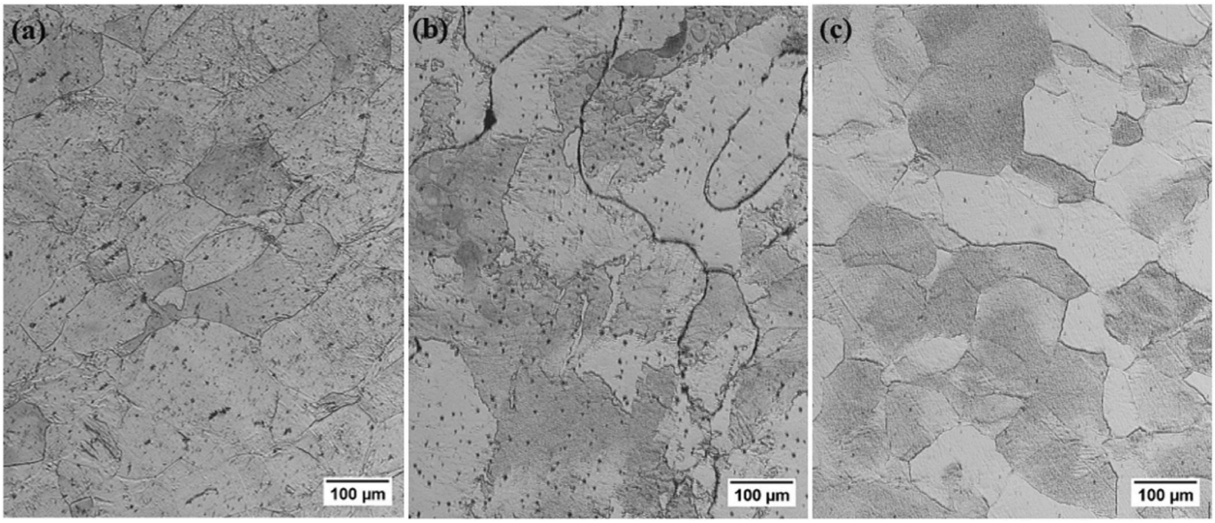

Fig. 2. Optical micrographs of hot-rolled alloys after etching in aqua regia: (a) FeCr, (b) FeCrY, and (c) FeCrTi.

It is worth mentioning that, in this study, AISI 430 and AISI 304 stainless steels were used to establish a comparison between Fe–Cr-X alloys and materials used in the industry, in order to have a better understanding of the potential of these alloys in relation to corrosion resistance. Thus, these two stainless steels were selected because they are widely used and have specific microstructural characteristics, where AISI 430 presents a ferritic matrix, which is also found in the alloys studied, and AISI 304 presents an austenitic matrix, which contains higher levels of Cr and especially Ni, thus offering greater resistance to corrosion compared to AISI 430. For these commercial stainless steels, it should be added that this comparison was carried out in "as received" condition, with AISI 430 having an average grain size of 11.8 ± 5.6 μm and AISI 304, 8.8 ± 3.7 μm, demonstrating that their average values are much lower than those obtained for the FeCr, FeCrY and FeCrTi alloys. However, when the relative percentage uncertainties of the grain sizes are taken into account, they are around 45% for the FeCr alloy and 54% for the FeCrY and FeCrTi alloys, which is not very different from what is observed in commercial stainless steels, with uncertainties of 48% for AISI 430 and 42% for AISI 304.

Regarding the effects of Ti and Y on the grain sizes of the alloys observed in Fig. 2, it can be seen that their additions (~0.2 wt%) were not enough to trigger an appropriate refinement of their respective microstructures, although satisfactory results have been seen at low concentrations for other alloy systems, as observed by Li et al. [29], who investigated $(Fe_{83}Ga_{17})_{100\text{-}x}Y_x$ (x = 0, 0.16, 0.32, 0.48, 0.64) alloys and showed that a small addition of 0.16 at.% was enough to significantly reduce grain size. This same effect was also observed in Ti alloys [30,31] and in Mg–5Li-3A1-2Zn-xY (x = 0, 0.4, 0.8, 1.2, 1.6, 2.0) alloys, whose smallest grain size was reached with 0.8 wt% [32]. For Ti, its role as a grain refiner in ferrous alloys is already well known in the literature [33–35]. Kang et al. [36], who studied UNS S44100 ferritic stainless steels with Ti contents between 0.10 and 0.50 wt%, observed that the average grain size decreased with increasing Ti concentration, which also enlarged the number of (Ti,Nb)(C,N) precipitates.

As previously reported, several precipitates were predicted for the FeCr, FeCrY and FeCrTi alloys in the thermodynamic simulations (Tables 2–4), with very low volume fractions, except for the σ phase (Fig. 1). In this respect, it is worth mentioning that Fig. 2 shows various dark spots, especially in the micrograph of the FeCrY alloy (Fig. 2b), which correspond only to chemical etching pits, since the sample surfaces were strongly etched by the aqua regia solution, given that its action time was increased so that all the grain boundaries could be revealed. Furthermore, as it will be discussed later, the precipitates identified in these alloys have sizes that are only seen at higher magnifications, such as those shown in Figs. 4–6, obtained by SEM, whose sample surfaces were etched in 10 vol% oxalic acid ($H_2C_2O_4$) solution.

Fig. 3 presents the XRD patterns of the FeCr, FeCrY and FeCrTi alloys, which only show peaks corresponding to α-Fe. Here, it is important to

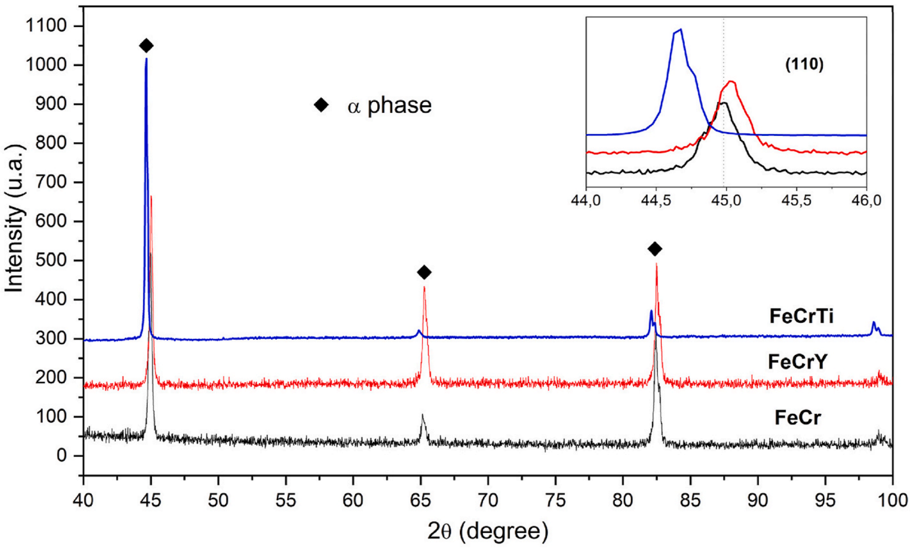

Fig. 3. XRD patterns of polished Fe–Cr-X alloys without etching. Peak shift illustrated for (110) plane in the inset.

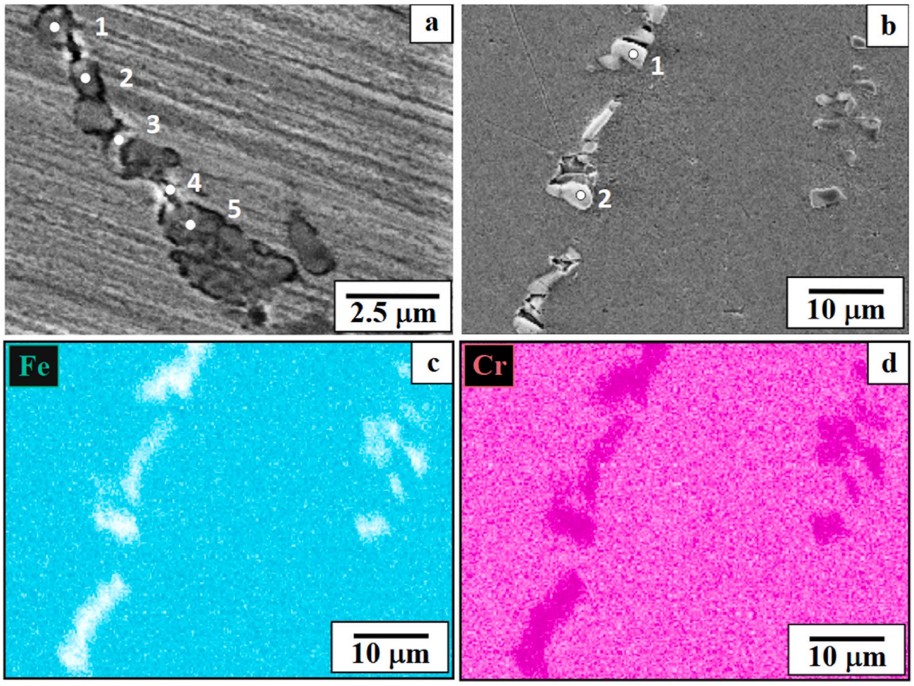

Fig. 4. SEM images of the FeCr alloy etched in 10 vol% oxalic acid ($H_2C_2O_4$) solution, showing the presence of precipitates in (a) and (b). X-ray (EDS) elemental maps of Fe–K (c) and Cr–K (d) are given for the image in (b), and points 1 to 5 in (a) and 1 and 2 in (b) correspond to the EDS analyses presented in Tables 5 and 6

point out that the detection limit of the technique is around 5% by volume [37], i.e., if any phase is present below this level, its peaks will not be detected above the noise in the diffraction pattern. Considering the volume fractions of the phases shown in Fig. 1, only the σ phase, in addition to α-Fe, could have its peaks noticed. In this case, the work of Biezma et al. [38] shows that one of the peaks of the σ phase coincides with the peak referring to the (110) plane of α-Fe, highlighted in the detail on the right of Fig. 3. Aside from this, in this study, the XRD were not obtained from powdered samples, and a certain preferential orientation must exist, which would make it even more difficult to identify the precipitates, thus requiring additional analyses.

Regarding α-Fe, the literature shows that this phase can present a lattice parameter of 2.867 Å [39] and even 2.839 Å [40]. For the FeCr alloy, the addition of 24.7 wt% Cr (Table 1), although high, resulted in a small change in the lattice parameter of the body centered cubic (bcc) Fe structure, which assumed a value of 2.856 Å, since there is little discrepancy between their atomic radius ($r_{Fe} = 1.26$ Å and $r_{Cr} = 1.28$ Å). When comparing the FeCr alloy with the FeCrTi alloy, which have basically the same Cr concentration (24.7 and 24.25%, respectively), there is an increase in the lattice parameter to 2.870 Å, even for an addition of 0.18 wt% Ti, which is attributed to its larger atomic radius of 1.47 Å compared to that of Fe, indicating that at least part of the Ti added to the FeCr alloy is dissolved in the α matrix. This is most evident in the detail on the right of Fig. 3, which shows a significant shift in the intensity peak of the crystalline plane (110) of the FeCrTi alloy, which takes on a lower value of 2θ. In this respect, the thermodynamic simulation shows that the Ti concentration is 0.06 wt % in the α-Fe phase at 660.8 °C (Table 4). For the FeCrY alloy, which has 24.71 wt% Cr

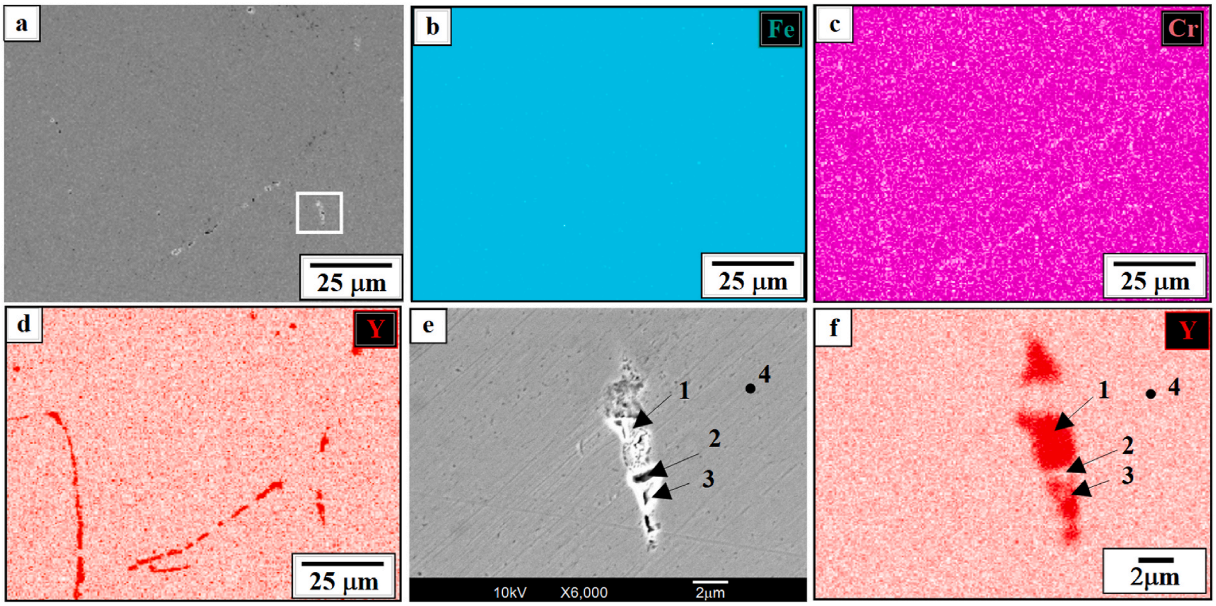

Fig. 5. SEM image of the FeCrY alloy etched in 10 vol% oxalic acid ($H_2C_2O_4$) solution, showing the presence of precipitates in the grain boundaries (a) and X-ray (EDS) elemental maps of Fe–K (b), Cr–K (c) and Y-L (d). The region delimited in (a) is seen magnified in (e), with its Y-L distribution map (f). Points 1 to 4 (e, f) correspond to the EDS analyses presented in Table 7.

(Table 1), the addition of 0.195 % Y brought virtually no change in its lattice parameter, whose value was 2.853 Å. In the Fe–Y system [41], the solubility limit of Y in the γ-Fe phase is considered to be lower than 0.6 at. % at approximately 1350.0 °C. In the α-Fe phase, its concentration is even more restricted, reaching a value of around 0.0016% at 827.0 °C and 0.0006% at 427.0 °C [42]. This condition of extremely low solubility was also predicted by ThermoCalc® for the FeCrY alloy, which presented a content of 8×10^{-5} wt % of Y in this phase at 666.2 °C, as shown in Table 3. Considering that the atomic radius of Y is 1.80 Å, if there were any solubility of this alloying element in the ferritic matrix, then this would lead to an increase in the lattice parameter of α-Fe, as already reported in the literature for nanocrystalline Fe–Cr–Y alloys [43], where the diffraction peaks shifted to lower 2θ positions. These observations about the effects of Ti and Y on the lattice parameters of the α phase of the FeCr alloy highlight the discussions about the corrosion resistance of these materials, as presented in sections 3.3.1 and 3.3.4.

In order to observe the precipitates, SEM/EDS analyses were carried out on the FeCr, FeCrY and FeCrTi alloys. Table 5 shows the chemical compositions of the precipitates found in a grain boundary region of the FeCr alloy, whose morphology is presented in Fig. 4a. Thus, it can be seen that these precipitates are rich in Cr (points 1 to 5) and also contain a C concentration of around 3.2%. When comparing the Cr concentrations in Table 5 with the results of the thermodynamic simulation, shown in Table 2, one can see that such contents are consistent with the formation of the σ phase, although these are a little lower and the presence of C can make this indication somewhat fragile. In this sense, one caveat should initially be made regarding the reliability of the numbers presented in Table 5, since EDS is a semi-quantitative analytical method and there is therefore an uncertainty in the measurement. Apart from the consideration of the instrument, in the case of particles, one should bear in mind that by placing the beam on them, a contribution from the surrounding matrix can be obtained, which can, in this situation, under-quantify Cr concentrations. As far as C is concerned, it is a fact that there is some limitation in detecting low atomic number elements due to the phenomenon of X-ray absorption, which occurs as a result of the Be window of the detector. That being said, it should not be neglected that, in several studies [38,44], the σ-phase nucleates in high-energy regions, advancing more rapidly at the grain boundaries. It has also been demonstrated that the presence of chromium carbides supports the nucleation of the σ phase due to chemical composition gradients [38,45]. Chen and Yang [45], for example, found $M_{23}C_6$ particles, with sizes around 0.1 µm, completely surrounded by the rod-shaped σ phase. In this context, Villanueva et al. [44] reported that σ particles tend to be elongated at first but take on a more rounded shape after saturation at the grain boundaries. This morphology with a globular appearance can be seen in Fig. 4a of the present study. Furthermore, for the FeCr alloy, it is predicted that $Cr_{23}C_6$ precipitation will occur before the σ-phase (Table 2), having a volume fraction of the order of 10^{-3}, as shown in the magnified region of Fig. 1a.

Another important fact is that the temperature at which the alloy was rolled, at 980.0 °C, provides suitable conditions for $Cr_{23}C_6$ precipitates to remain. According to Cardoso et al. [46], at temperatures close to 1100.0 °C, diffusion is still relatively slow and there is no complete dissolution of all the carbides. Considering that part of these carbides is dissolved, the C atoms, which present a higher diffusion coefficient, migrate more easily to the interior of the grains, leaving behind regions with high concentrations of Cr that could become sites for σ nucleation. In the case of hot working, it can also be seen that recrystallization itself creates thermodynamic conditions for the occurrence of several precipitates, mainly the σ phase [47]. Thus, one can assume that the C content presented in Table 5 is related to tiny particles of $Cr_{23}C_6$ dispersed within the σ-phase, as observed by Chen and Yang [45].

Also regarding the FeCr alloy, Fig. 4b shows the existence of precipitates rich in Cr and poor in Fe, as observed in the element distribution maps (Fig. 4c–d). From Table 6, it can be verified that their Cr concentrations are higher than those found for the σ phase. In addition, their Fe concentrations, at around 8.3 wt %, although possibly contributed by the surrounding matrix, and the presence of C, show that these are $Cr_{23}C_6$ precipitates. This understanding becomes clearer when comparing these results with the concentrations predicted by thermodynamic calculations at 663.9 °C (Table 2). Regarding Cr_2O_3 and Cr_2N, which were also predicted in the simulation, there was no evidence of the formation of these phases. Here, it is worth highlighting that their volume fractions presented values in the order of 10^{-4} (Fig. 1a).

For the FeCrY alloy, a much greater number of precipitates can be seen located on the grain boundaries, as shown in Fig. 5. Its element distribution maps (Fig. 5b–d) show that these precipitates are predominantly Fe and Y rich. In the case of Cr (Fig. 5c), only a few faint lines

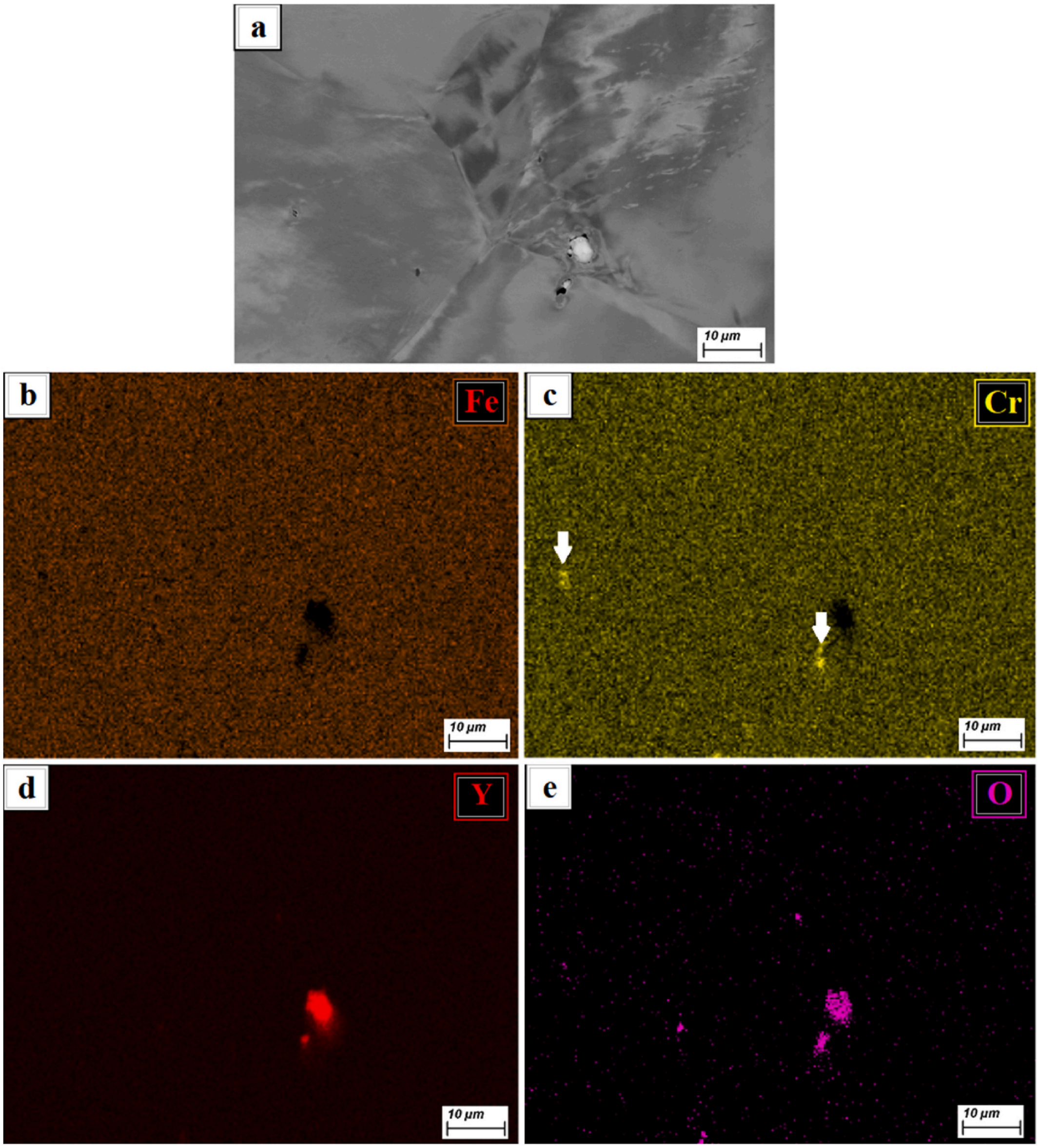

Fig. 6. SEM-BSE image of the FeCrY alloy etched in 10 vol% oxalic acid ($H_2C_2O_4$) solution (a), and X-ray (EDS) elemental maps of Fe–K (b), Cr–K (c), Y-L (d) and O–K (e). In (c) some Cr-rich precipitates are indicated by arrows.

Table 5
EDS results (wt%) for precipitates in the grain boundary region of the FeCr alloy, shown in Fig. 4a.

Point	Fe	Cr	C
1	63.0	34.4	2.6
2	53.0	44.2	2.9
3	62.7	33.4	3.9
4	58.7	38.2	3.1
5	61.1	35.6	3.4

Table 6
EDS results (wt %) for precipitates of the FeCr alloy shown in Fig. 4b.

Point	Fe	Cr	C
1	7.9	90.8	1.3
2	8.7	90.1	1.1

slightly depleted of this element are observed in the same places where Y stands out (Fig. 5d). In order to better identify the precipitates, a region was selected for quantifying the elements, which corresponds to the area delimited by a square in Fig. 5a, and is shown at a higher magnification in Fig. 5e. The Y distribution map of the region analyzed was also obtained and is shown in Fig. 5f. Thus, EDS analyses show that points 1 and 3 (Table 7) have Y contents of 15.4% and 12.1% respectively, which contrasts with the ferritic matrix (point 4), where Y was not detected. Table 3 indicates that these precipitates correspond to $Fe_{17}Y_2$, since the other Y-rich phases (YN and Y_2O_3), predicted in the simulation, have

Table 7
EDS results for the precipitates (points 1 to 3) and for the α-Fe matrix (point 4) of the FeCrY alloy, wt. %.

Point	Fe	Cr	Y
1	67.7	16.9	15.4
2	42.6	50.0	7.4
3	65.8	22.1	12.1
4	76.2	23.8	0.0

much higher contents of this alloying element (>70 wt%). In the literature, the presence of $Fe_{17}Y_2$ was observed in the studies by Muthaiah et al. [43], who analyzed the Fe–15Cr–1Y alloy after heat treatment at 1000.0 °C for 1 h, and by Wang et al. [48], for the annealed Fe–13Cr–6Al–2Mo-0.5Nb-0.15Zr-0.2Y alloy. Although the thermodynamic simulation results show that there is no solubility of Cr in this phase (Table 3), He et al. [49], on the other hand, state that Cr can reach a maximum value of 18 at. % at 500.0 °C.

Taking point 2 of Table 7 into account, there is also a precipitate with a high Cr content, which is consistent with the σ-phase observed in the FeCr alloy. This phase, as previously discussed, is also expected for the FeCrY alloy (Table 3). Its Y concentration of 7.4% is due, in this case, to interference from the Y-rich precipitates that surround it, and its elongated shape, seen in Fig. 5e, is in accordance with the studies by Villanueva et al. [44] and Chen and Yang [45], suggesting that this phase is at a less advanced stage than that of the FeCr alloy.

The grain boundaries where the $Fe_{17}Y_2$ and σ phases were precipitated, as indicated in Fig. 5 and Table 7, are probably related to the better-defined grain boundaries observed in Fig. 2b, which were easily revealed by the chemical etching in aqua regia solution, but due to the longer time in this medium in order for the other grains to be revealed as well, resulted in deeper grooves. These locations that were more prone to the formation of secondary phases may be associated with boundaries where there is a greater misorientation angle between adjoining grains, since it has been observed that these are more susceptible to presenting a higher segregation of elements [50,51], which may be strong enough to promote the formation of secondary phases [52].

A backscattered electron image of another region also showing grain boundaries (Fig. 6a) indicates the presence of precipitates rich in Y and O, as shown in Fig. 6d and e, respectively. It is also noticeable that Fe and Cr are basically non-existent in these same locations (Figure b–c), which points to the fact that they are Y_2O_3 precipitates. Their volume fraction is extremely low based on thermodynamic simulation, in the order of 10^{-4}, while for $Fe_{17}Y_2$, this value is 10^{-3} (Fig. 1b). In this respect, it should be mentioned that there is a strong affinity of Y with O [53], whose content of this element is (0.015 ± 0.001) wt.% in the FeCrY alloy.

Some Cr-rich precipitates, indicated by arrows in Fig. 6c, are also observed, one of which was formed adjacent to a Y_2O_3 precipitate, close to the grain boundary. The STEM analysis in the annular dark field (ADF) mode of the FeCrY alloy (Fig. 7) shows, through the element distribution maps (Fig. 7b–c), the existence of two types of Cr-rich precipitates: one poor in Fe, exemplified by a yellow dotted line, being more dominant in the analyzed region, which must correspond to $Cr_{23}C_6$, despite the impossibility of analyzing C; and another rich in Fe, exemplified by a white dotted line, which is believed to be the σ phase. In this case, it should be pointed out that its morphology is consistent with the elongated aspect observed for the same phase identified in

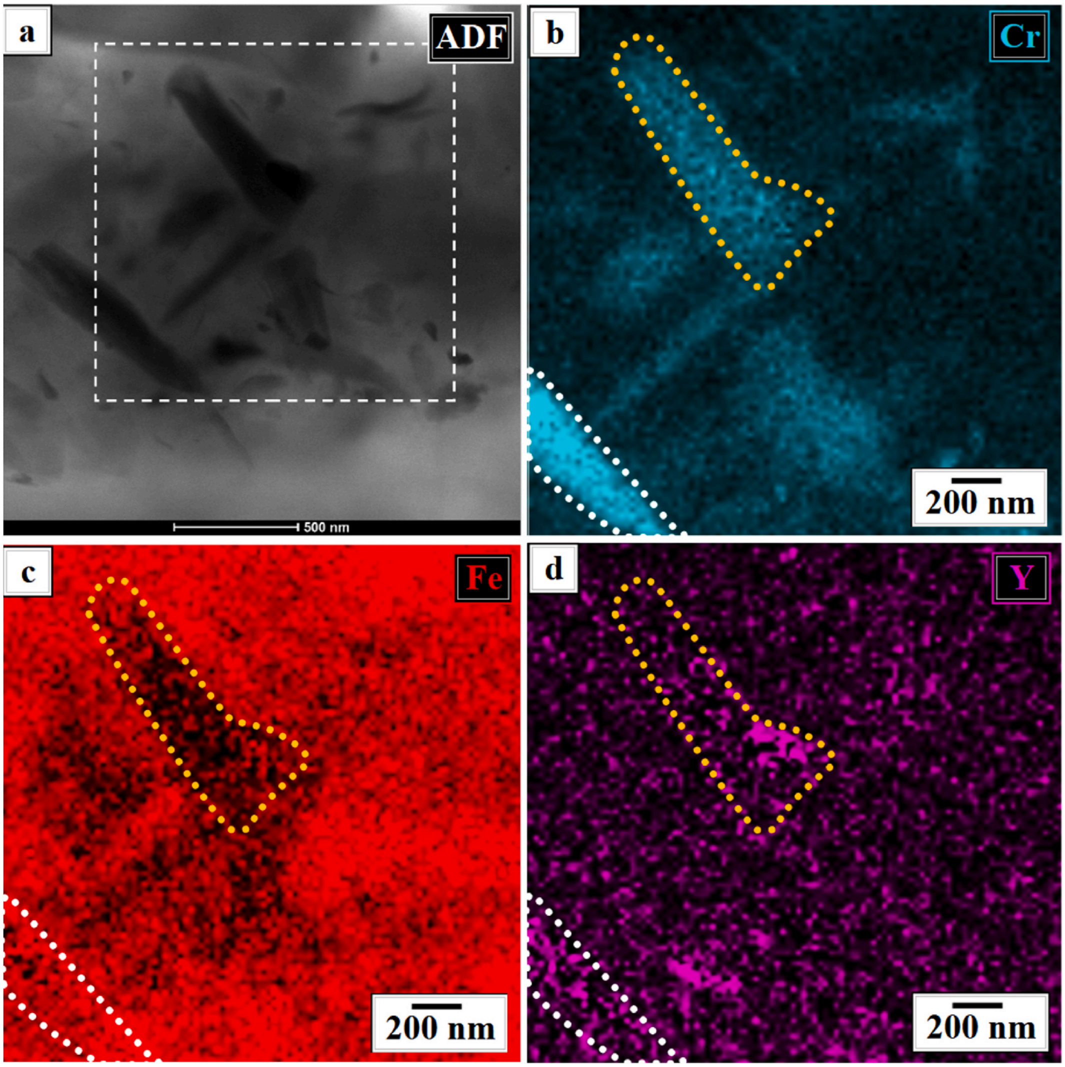

Fig. 7. STEM image in ADF mode for FeCrY alloy (a) and X-ray elemental maps of Cr–K (b), Fe–K (c) and Y-L (d) of the region delimited in (a).

Fig. 5e.

The Y distribution map (Fig. 7d), in turn, shows the presence of Y-rich precipitates with a morphology not well defined, and with sizes smaller than 165 nm, which can be attributed to Y_2O_3, identified in Fig. 6. Their sizes are much smaller than those observed in Fig. 6a, of 1.6 and 4.7 μm, but since plastic deformation in ferritic alloys is complex and inhomogeneous, as discussed previously, the smaller Y_2O_3 precipitates observed in this region may be due to a more pronounced fragmentation. In this sense, the thermodynamic simulation indicates that Y_2O_3 is formed at 1098.7 °C (Table 3), which shows that this oxide remains stable during rolling at 980 °C of the FeCrY alloy. Regarding the process of deformation and recrystallization of secondary phases, it can be seen that when slip systems are activated, these phases initially block the dislocation movements, leading to a high concentration of stresses. In the case of Y_2O_3, the large difference in the modulus of elasticity between the matrix and its precipitates results in irregular deformation [53] and, in such circumstances, the high concentration of local stress around the precipitates promotes cracks in those with greater thickness. This gradual breakdown of the coarse precipitates due to the propagation of cracks during plastic deformation subsequently causes a process of spheroidization as a way of minimizing the surface energy of these fragmented precipitates. In this case, it is also observed that their distribution in the matrix becomes more homogeneous [54].

For the FeCrTi alloy, one could notice the presence of some rounded precipitates dispersed in the α-Fe matrix, indicated as points 1 and 2 in Fig. 8. Considering their Ti, C and N contents, presented in Table 8, it can be said that these are titanium carbonitrides of the Ti(C,N) type, as shown in Table 4. To this fact, it should be added that Ti controls the interstitials in stainless steels, which allows the precipitation of stable compounds such as TiN, TiC and $Ti_x(C,N)_y$ that, in turn, inhibit the formation of chromium carbides that are highly detrimental to corrosion resistance [55]. In the case of the FeCrTi alloy, the concentrations of the elements are different from those presented in the thermodynamic simulation (Table 4). In this respect, it is important to make two considerations: (1) low atomic number elements, such as C and N, present a certain limitation in relation to detection by EDS, and the surrounding matrix also contributes in the case of particles, as previously reported, and (2) the C and N contents themselves undergo quite significant changes as the temperature decreases, as it can be seen by comparing their values at 1345.1 and 660.8 °C, where an inversion is noted, with the highest temperature presenting a higher concentration of N in comparison to C, leaving unclear which contents were assumed in non-equilibrium conditions. In this sense, the EDS results for these elements are consistent with the expected (C > N), since the FeCrTi alloy has 0.021 wt % of C and 0.0003 wt % of N (Table 1).

Table 8
EDS results for precipitates of the FeCrTi alloy, wt. %.

Point	Fe	Cr	Ti	C	N
1	66.1	20.8	6.7	6.0	0.4
2	61.1	19.0	15.1	3.8	1.1

From thermodynamic calculations, the formation of Ti_2O_3 is also expected, but this oxide was not detected in the α-Fe matrix. In this case, it should be noted that its volume fraction is estimated to be in the order of 10^{-4}, which is lower than that corresponding to Ti(C,N), whose value is 10^{-3}. Regarding the σ phase, its precipitation was not identified by SEM/EDS, unlike the FeCr and FeCrY alloys. In this respect, studies have considered that Ti accelerates its formation [56,57]. According to Blachowski et al. [7,8], this process occurs for Ti contents ≤1.5 at. %, with the highest rate for alloys containing 0.3 at. % Ti. However, Vasilyuk and Butenko [58], taking into account electronic vacancy calculations, suggested that Ti delays the formation of σ. In this aspect, it can be said that the results presented for the FeCrTi alloy seem to converge with this understanding, although Fig. 1c points to a contrary prediction. Thus, in order to clarify any doubts about the existence of this phase, a more detailed analysis was carried out by TEM.

Fig. 9 shows the TEM micrograph of this alloy in bright field (BF) mode and the corresponding selected area diffraction (SAD) in ring pattern shape in the top right corner. It can be seen from this figure that only a labyrinth-type structure is present, which is developed by the movement of dislocations in two or more slip systems, giving origin to two sets of presumably perpendicular dipolar walls, according to Boulanger et al. [59]. This structure is typical of dislocation substructures in the form of persistent slip bands (PSBs), which must have been produced during rolling at 980.0 °C. Here, it is worth highlighting that the driving force for static recrystallization tends to be reduced during the hot deformation of α-Fe, as discussed previously.

In the case of labyrinth structures, Tjong [60] observed similar substructures in the cyclic deformation of Fe–25Cr-(2–4)Al and Fe–19Cr–4Ni–2Al alloys, and pointed out that C has a strong influence in b.c.c. metals and alloys. In this sense, Mughrabi et al. [61] consider that the C in α-Fe is responsible for reducing the mobility of non-screw dislocations to that of the screw dislocations, which could result in the existence of very dense primary edge multipole structures. From Fig. 10, which presents STEM-HAADF images (high-angle annular dark field) in Z-contrast mode of the FeCrTi alloy, one can also observe subgrains distributed throughout the microstructure with sizes of around 1 μm. Inside the α-Fe phase subgrains (Fig. 10b), there are still many slip

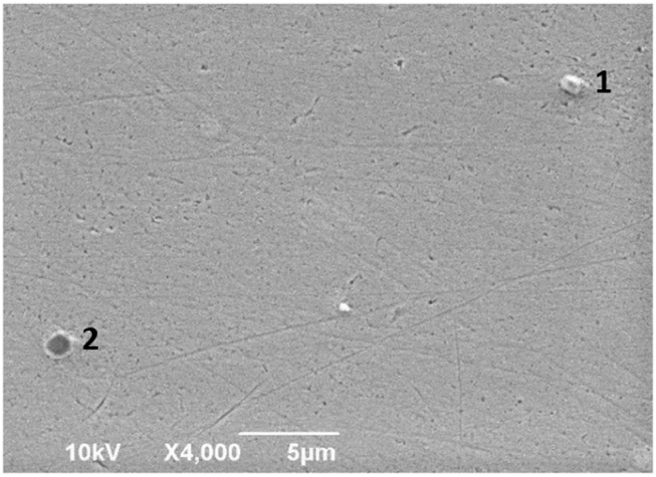

Fig. 8. SEM image of the FeCrTi alloy etched in 10 vol% oxalic acid ($H_2C_2O_4$) solution, showing the presence of precipitates in the α-Fe matrix.

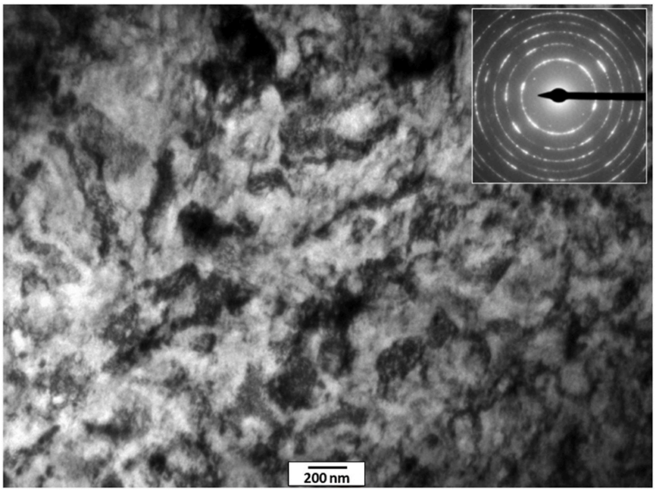

Fig. 9. TEM micrograph in BF mode of the FeCrTi alloy with its respective SAD showing a labyrinth-type structure.

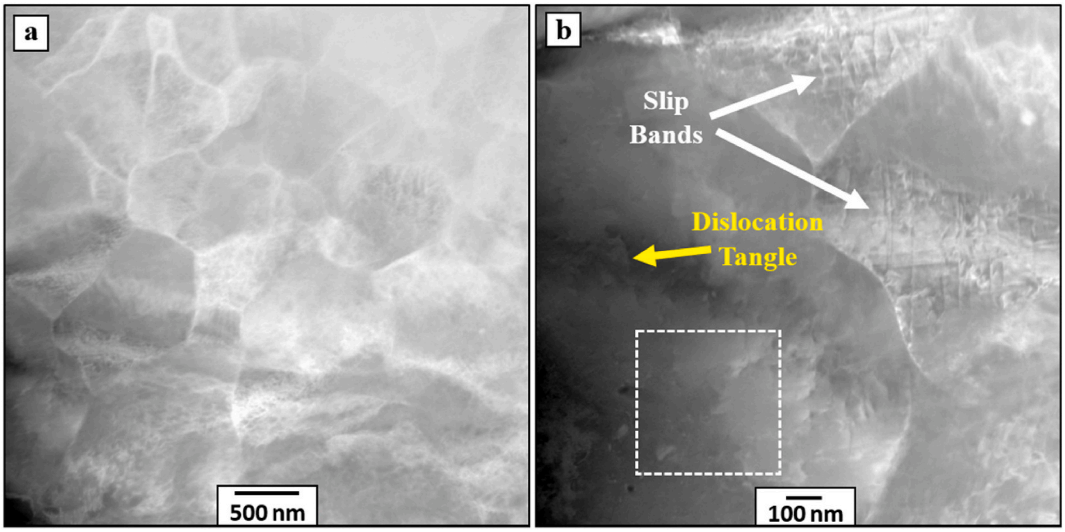

Fig. 10. STEM-HAADF images in Z-contrast mode of the FeCrTi alloy, showing in (a) subgrains of the α-Fe phase with sizes around 1 μm and, in (b), the presence of slip bands and dislocation tangles. The delimited region (white dotted line square) is presented in the sequence (Fig. 11) at higher magnification, together with X-ray (EDS) elemental maps.

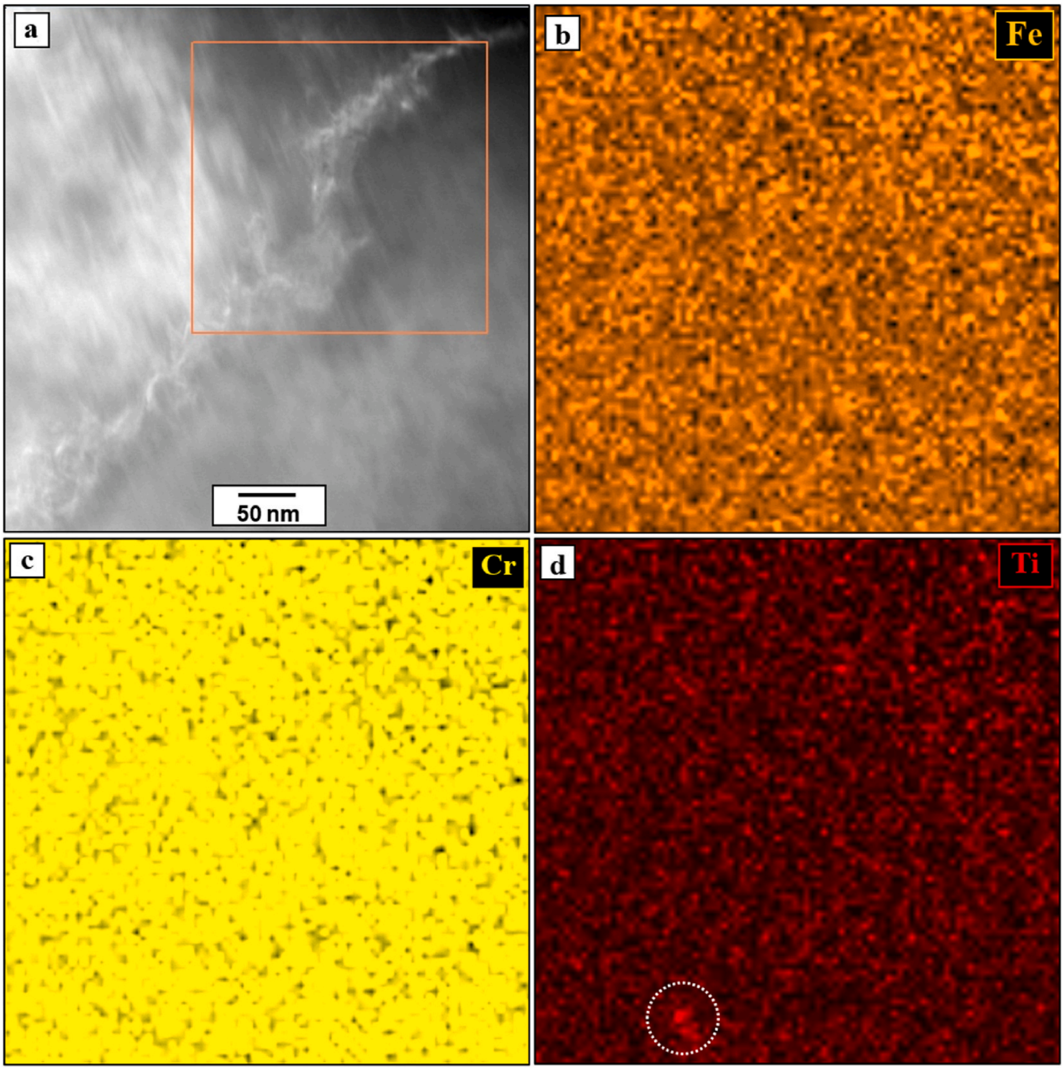

Fig. 11. STEM-HAADF image in Z-contrast mode of the FeCrTi alloy in (a), and X-ray (EDS) elemental maps of Fe–K (b), Cr–K (c) and Ti–K (d) of the region delimited in (a), showing nanometric regions around 6 nm with Ti enrichment.

bands, as well as dislocation tangles, as observed by Li et al. [62]. According to Tjong [60], the agglomeration of these tangles can lead to loop patches, which are also considered to be dislocation substructures.

In order to further investigate the issue of the σ phase, element distribution maps were obtained, since this phase is rich in Cr. The results, however, only pointed to another type of precipitation. Thus, it can be seen in Fig. 11, which corresponds to the magnified region delimited in Fig. 10b, that there are nanometric-sized regions, around 6 nm, with Ti enrichment which, due to the presence of C in the alloy, may correspond to nanometric TiC carbides dispersed in the α-Fe matrix. This fact, associated mainly with the non-occurrence of σ precipitation, provides a promising response from a corrosion point of view. Therefore, it can be said that the low concentration of Ti (~0.2 wt%) in the FeCrTi alloy was sufficient to inhibit its nucleation. In this context, it is observed that the concentration and type of alloying element play a fundamental role in the appearance of this phase. Zhang et al. [63], for example, found that increasing the concentration of N prevents the formation of σ in super austenitic stainless steels. On the other hand, in the case of Mn, a higher content of this element (from 10.95 to 16.79 wt %) promotes a significant increase in its precipitation rate in duplex stainless steels [62], which is attributed to the fact that higher levels of Mn and Cr participate in its formation.

3.3. *Corrosion resistance*

3.3.1. *Anodic polarization curve*

Anodic polarization curves of FeCr, FeCrY and FeCrTi alloys, as well as of AISI 430 and AISI 304, are shown in Fig. 12. A current plateau is observed in all samples, characterizing a behavior typical of that which undergoes passivation alloys. It is important to highlight that all alloys in this study present high Cr content in their compositions, as seen in Table 1, and this element is essential for the formation of a resistant and stable oxide layer. In the case of stainless steels, the minimum Cr concentration at which oxide formation with good protective properties can be observed is 10.5 wt%, according to the EN 10088-1 [64]. The alloys produced for this study have a higher Cr content, which explains their better performance when compared to commercial alloys.

Although the approximate values of the corrosion potentials (E_{corr}), obtained in the OCP, are very close for all samples, namely FeCr (−0.152 V), FeCrY (−0.147 V) FeCrTi (−0.149 V), AISI 430 (−0.179 V) and AISI 304 (−0.1778 V), Fig. 12 depicts that the FeCrTi alloy presents a broader and better-defined passive region than the other ones. This behavior is indicative that the Ti contributes to the formation of a more stable and resistive oxide. Based on the polarization curve profiles, oscillations and instability in the current were observed, especially for the FeCrY alloy. Such an event may be related to the competition between the formation and nucleation of metastable micro-pitting and repassivation process of the protective oxide.

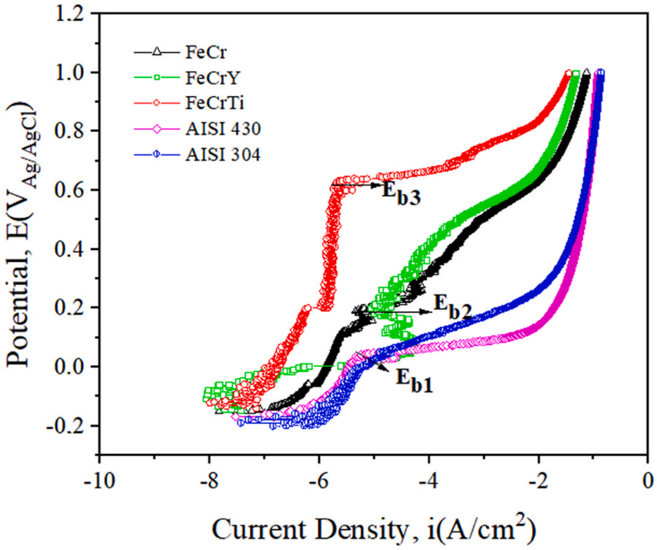

Fig. 12. Anodic polarization curves of commercial steels and Fe–Cr-X alloys in 3.5 wt% NaCl solution without agitation and at RT.

Overall, this behavior is observed before the sudden increase in current, which is related, many times, to the formation of stable pitting on the surface. The potential at which the current density sharply increases is known as breakdown potential (E_b) [65–67]. Although most samples do not have a well-defined breakdown potential, it is possible to identify the approximate values where the current increases most abruptly. For the commercial alloys, this potential is marked in Fig. 12 as E_{b1}, for the FeCr and FeCrY alloys as E_{b2} and for the FeCrTi alloy as E_{b3}. The composition containing Ti has the highest E_b, and the passive range (ΔE) is significantly larger compared to the other alloys. Thus, given the fixed Cr content in the three compositions (close to 25 wt %), it is possible to say that the elements Y and Ti are responsible for microstructural changes that have a direct influence on corrosion resistance. Indeed, the FeCrTi alloys show anodic curves shifted to lower current density values when compared to the FeCr alloy curve. On the other hand, the FeCrY alloy behaves in a similar way to the FeCr alloy, although it has lower current densities and is more unstable in general. Fig. 12 shows greater current instability up to approximately 0.460 V. This behavior may refer to the dissolution of the layer due to the localized action of chloride ions with the formation of metastable pits, as discussed above. This event is often observed in stainless steels and FeCr alloys [65–67].

Another possibility for this behavior is the microstructural effect of the alloy. According to West [68], who has assessed the electrochemical behavior of stainless steel in highly alkaline medium, the anodic polarization curve derives from the overlapping of the effects of several phases observed in the material the more heterogeneous the microstructure, more anodic current peaks can emerge. Based on the microstructural analysis of the FeCrY alloy presented in sections 3.1 and 3.2, it was observed that this alloy has quite heterogeneous microstructure. The thermodynamic simulation results show that the addition of Y to the FeCr alloy generated a very complex microstructure, with the presence of several precipitates, as shown in Table 3. The σ, $Fe_{17}Y_2$, Y_2O_3 and $Cr_{23}C_6$ phases were identified, the latter two being found in lower volume fractions, especially when compared to the σ phase. It is important to note that the other ferrous alloys also showed microstructures with more than one phase. However, the current oscillation was lower, especially for the FeCrTi alloy. The FeCr alloy also showed the σ-phase, as well as particles of chromium carbides ($Cr_{23}C_6$). However, the corrosion behavior observed in this alloy is certainly more influenced by the σ phase, which has a higher volume fraction than that of $Cr_{23}C_6$, according to the thermodynamic simulation (Fig. 1a). These phases are also rich in Cr and deplete the adjacent matrix of this element, thus worsening corrosion resistance of the alloy [69]. On the other hand, the alloy containing 0.18 wt % Ti showed only Ti (C,N) precipitates dispersed in the α-Fe matrix and a nanometric precipitation attributed to TiC, as shown by the SEM/EDS and TEM results (Figs. 8 and 11). These precipitates favor the corrosion resistance of the material because they inhibit the formation of the σ phase [69].

After the anodic polarization assays, the surfaces of all alloys were assessed through scanning electron microscopy to confirm the presence of localized forms of corrosion and justify the current density increase. Although all alloys have presented this corrosion form, a more discerning investigation was carried out in alloys produced for the present study through images of secondary electrons, as shown in Fig. 13a–i. The FeCr alloy presented a surface with several pitting (with different diameters), as shown in Fig. 13a–b. Detail 1, in Fig. 13b, makes it possible to observe the existence of micro-pitting inside the larger pitting. Although pitting is the main form of corrosion observed on the surface of the alloy, the formation of pitting in the grain boundary

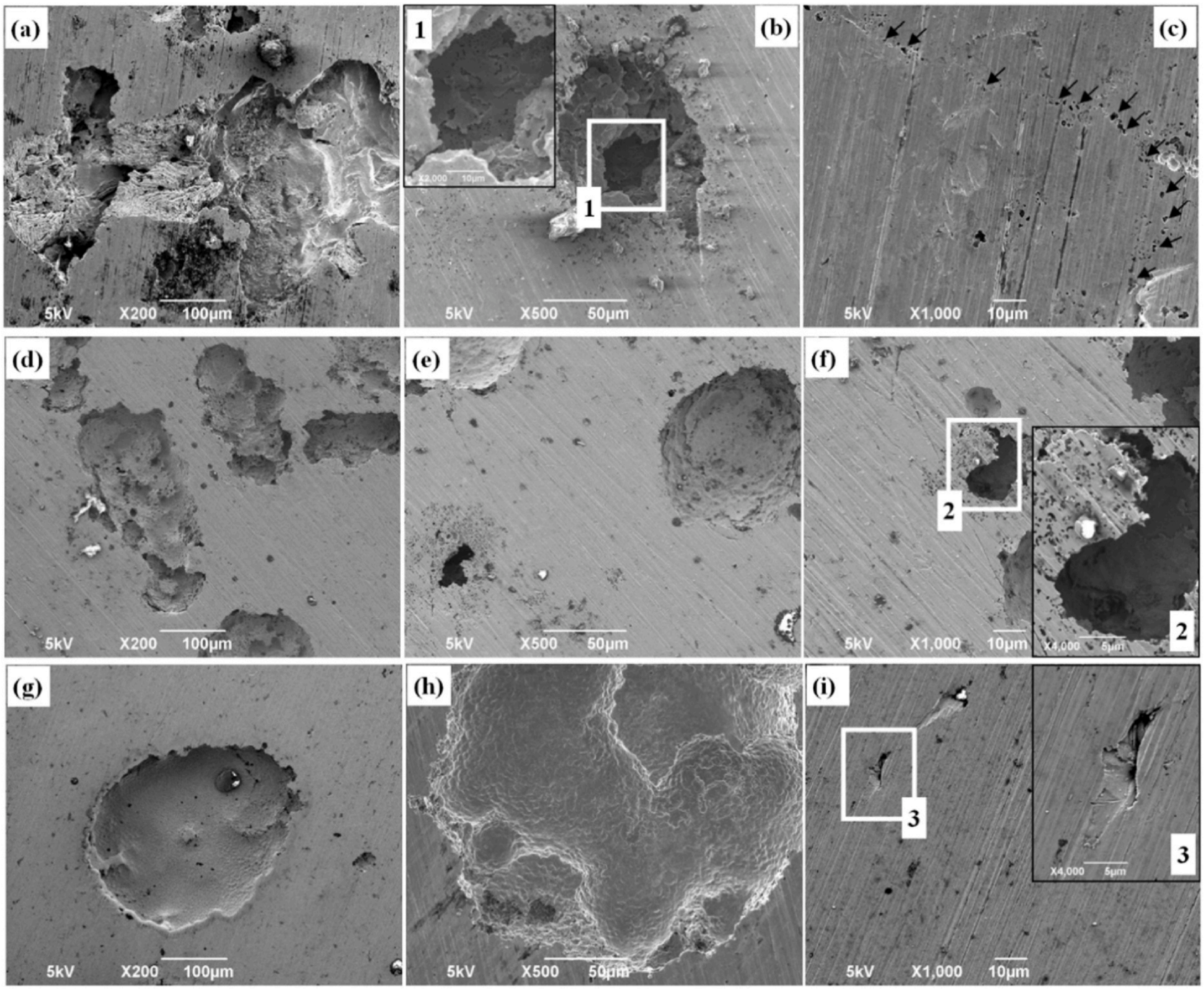

Fig. 13. SEM micrographs of alloys after anodic polarization tests: (a–c) FeCr, (d–f) FeCrY and (g–i) FeCrTi. Details 1, 2 and 3 show the emergence of pitting under higher magnification.

regions cannot be ignored, as seen in Fig. 13c. This image suggests the occurrence of intergranular corrosion, albeit in its initial phase. This fact cannot be overlooked since the microstructure showed the presence of the σ phase that nucleates in a high-energy region, advancing more rapidly towards the grain boundaries. The literature outspreads indicates that the main intergranular corrosion mechanism in stainless steels happens through the formation of carbides at grain boundaries. However, the results show that, in this case, the σ phase plays a more important role for intergranular corrosion, since chromium carbides identified in this alloy revealed that the volume fractions are much lower than the σ phase, as expected in thermodynamic simulation.

The images of the FeCrY alloy in Fig. 13d–f shows pitting with larger diameters than those observed for the FeCr alloy. Detail 2, in Fig. 13f, shows the existence of micro-pitting inside the larger pitting. However, the detail also highlighted that the smaller pits agglutinate and compromise large areas of the material. As already discussed, the FeCrY alloy showed, in addition to the σ-phase, the $Fe_{17}Y_2$ precipitate, both located at the grain boundaries (Figs. 5–7). However, it is important to remember that although these phases were observed in higher volume fractions than the others formed in this alloy, small particles of $Cr_{23}C_6$ were also found, which were formed adjacent to a precipitate of Y_2O_3, close to the grain boundary. However, based on the established polarization conditions, there were no regions featuring intergranular corrosion in this alloy, although the existence of phases with different compositions located at the grain boundaries points to the likelihood of this type of corrosion to be occurring. This heterogeneity can lead to significant differences between potentials of phases found in this grain-boundary region, since there are phases richer in Cr and other phases richer in Y and Fe. Standard reduction potentials of the elements observed in alloys are presented below:

$$Fe^{2+} + 2e^{-} \leftrightarrow Fe^{0}\ E^{0} = -\ 0.440\ V$$

$$Cr^{3+} + 3e^{-} \leftrightarrow Cr^{0}\ E^{0} = -\ 0.740\ V$$

$$Y^{3+} + 3e^{-} \leftrightarrow Y^{0}\ E^{0} = -\ 2.370\ V$$

Cr and Y present reduction potentials less noble than Fe. However, it is known that Cr has passive behavior in several aggressive media due to the protective profile of its oxide. The standard reduction potential of Y is yet more negative than Cr, but the literature about the electrochemical behavior of this element in ferrous alloys is scarce. Because FeCrY alloy precipitates are mainly located in grain boundaries, intergranular corrosion must not be neglected in this material; therefore, it must be further investigated.

Studies available in the literature about the effect of the addition of Y on the resistance to corrosion mostly lead towards Mg alloys. Some other authors reinforce the benefit of the addition of this element to increase resistance to corrosion, but others report that Y is only beneficial in solid solution. Nevertheless, when it forms precipitates, it gives negative contribution to resistance to material corrosion due to the formation of galvanic microcells [70,71].

This behavior is similar to what happens in the FeCrY alloy, although studies on Y in ferrous alloys with high Cr concentrations are scarce in the literature, especially regarding corrosion resistance [72]. However, the anodic polarization curves show that Y contributes, albeit slightly, to improve the corrosion resistance of the FeCr alloy. This effect will be further investigated through chronoamperometry and EIS tests.

Finally, Fig. 13g–i presents images of FeCrTi alloy surface after polarization. Again, images corroborated the electrochemical behavior in this material (Fig. 12). The best performance indicated by the higher breakdown potential, the wider passivation range and the lower current density values are factors that reflect a more defect-free layer on the metal surface. This behavior can be justified by the absence of the σ phase and the formation of TiC and Ti(C,N) precipitates in the α-Fe matrix, as discussed previously. These precipitates are more stable and inhibit the appearance of Cr-rich carbides, improving the corrosion resistance of this material [70,73].

Another important fact that may have contributed to improve the performance of this alloy lies on Ti solubility in the α-Fe matrix. According to the X-ray diffractogram (Fig. 3), there was a shifting of the peaks to smaller 2θ positions in α-Fe phase, which indicates increase in the Fe lattice parameter as the consequence of Ti atoms dissolution in Fe-based solid solution. However, the same was not observed for the Y, where there was the formation of precipitates rich in this element. The fact that part of Ti remained in the matrix, while part of it was consumed for the formation the nanometric TiC and Ti(C,N) precipitates, reduced the possibility of galvanic microcell formation and improved the resistance to corrosion in the material.

3.3.2. Chronoamperometry

Chronoamperometry assays were carried out to gather more information on the nature of the protective oxide of the alloys in this study. Based on the anodic polarization curve, the selected potentials were 0.100 V (in the passivation region common to all alloys), 0.180 V (close to the FeCr and FeCrY alloys breakdown potential) and 0.600 V (close to the break potential for FeCrTi alloys). Fig. 14 shows the current transient results (I versus t) for the alloys at the potentials determined above.

Fig. 14a presents the anodic current density response at potential of 0.100 V. Based on Fig. 12, the first chosen fixed potential, E = 0.100 V, is relatively close to the breakdown potential region of commercial stainless steels. It explains why commercial steels are the only ones showing significant current increase, which was followed by a stationary current density region that is most clearly observed from 2400 s assay time. This behavior indicates that defects have been generated in the oxide layer. Based on the applied potential of 0.100 V, the defects that occur on the surface of these alloys would be pitting growth. However, it is important to point out that the highest current values are attributed to AISI 430, which suggests that a larger number of well-developed pitting must be found in this material. This behavior corroborates the results presented in the anodic polarization curves and is associated with the higher Cr content present in AISI 304, as well as the presence of Ni.

On the other hand, FeCr and FeCrY alloys show basically no variations in current density up to approximately 2100 s. However, at times longer than this, currents started to slowly increase, suggesting that the first defects start to appear in the oxide layers. It is worth highlighting that these alloys have higher E_b than do commercial steels. The current responses presented in these materials, when they are subjected to fixed potential E = 0.100 V, have shown that the oxide layers in FeCr and FeCrY alloys are quite stable, and they provide better protection to the alloys. An even more interesting behavior was observed for the FeCrTi alloy. The current density remained at close to zero throughout the whole assay, which suggested a much more resistant and stable oxide formed on the surface of the material. It is important to recall that the breakdown potential (E_b) of this alloy is significantly higher than the applied potential, and it is indicative of the best resistance to localized corrosion among all materials tested under the assessed conditions.

The anodic current density response at the potential of 0.180 V can be observed in Fig. 14b. Initially, it the same behavior at the potential of

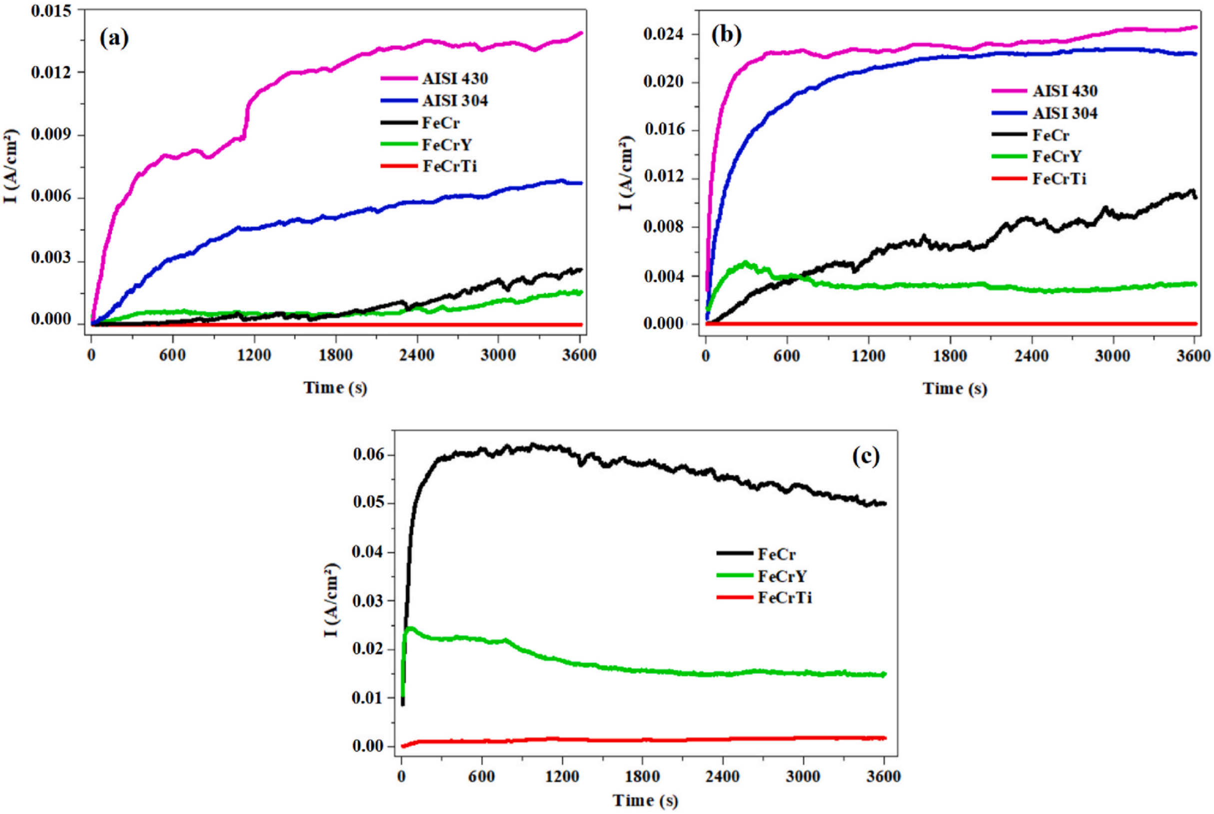

Fig. 14. Chronoamperometric curves of commercial steels (a,b) and Fe–Cr-X alloys (a–c) at constant potentials of 0.100 V (a), 0.180 V (b) and 0.600 V (c) monitored for 1 h.

0.100 V was noted, in which, once more, commercial steels recorded the highest current densities they were followed by those of FeCr, FeCrY and FeCrTi alloys. It is important to have in mind that the applied potential was slightly above the breakdown potential of commercial steels. Therefore, it was possible to observe a drastic increase in currents in these materials, in approximately 300 s after assay-start. Later, the current reached stability, mainly in AISI 304. Once more, AISI 430 presented higher current density values than the other alloys. Under these conditions and according to the curves, one could expect that pitting had been effectively formed on the commercial steels.

Regarding the FeCr alloy, it was possible to observe unstable behavior and a continuous increase in current during all the tests. On the other hand, the FeCrY alloy presented current increase at the beginning of the test, reaching a maximum value at approximately 300 s. The stability of current is observed around 1000 s. According to Park et al. [74], this behavior can be attributed to active-area reduction on the electrode surface due to passive film growth. Although the behavior of FeCr and FeCrY alloys were similar at a potential of 0.100 V, at a higher potential, current steady state was reached faster for the FeCrY alloy. The decrease in current followed by the plateau indicates that at this potential the growth kinetics of the passive film overlaps with the dissolution kinetics [75]. Thus, the presence of Y seems to have contributed to the formation of a more stable and resistive oxide film than that formed on the FeCr alloy. On the other hand, the FeCrTi alloy, once more, led to current close to zero throughout the test. This behavior highlighted the ability of this alloy to form and maintain the passive film.

Finally, the anodic current density response at 0.600 V was observed in Fig. 14c. The evolution of the current at this potential was only observed for the Fe–Cr-X alloys, in order to further investigate the effects of the Ti and Y elements. The influence of Y on resistance to corrosion in the FeCr alloy became more perceptible at higher potentials. There is a

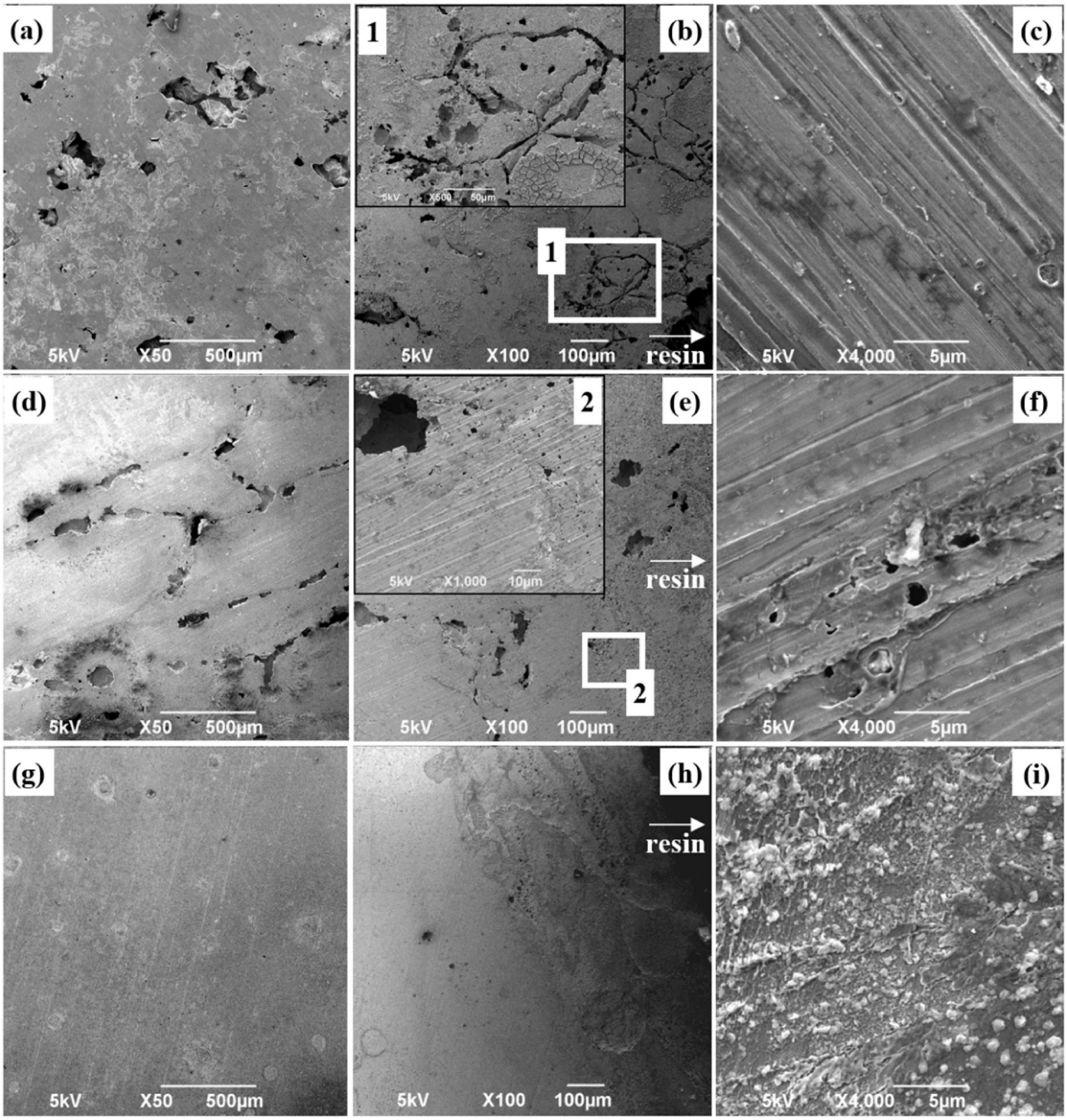

Fig. 15. SEM micrographs of alloys after chronoamperometric tests at constant potential of 0.600 V monitored for 1 h: (a–c) FeCr, (d–f) FeCrY and (g–i) FeCrTi. Details 1 and 2 show pitting under higher magnification.

clear separation among curves at 0.600 V, and it pointed out that the FeCr alloy reached current steady-state at higher values. It is known that the higher the potential, the easier the chloride ions to be attracted to electrode surface. Therefore, the aggressiveness of these ions will be more effective on films less resistive and in an initial state of formation; consequently, the current tends to rise [72]. This behavior reinforced the statement that the presence of Y somehow contributes to the protective effect of the formed oxide layer, since the current reached the steady-state at lower currents. The beneficial effect of Ti is unquestionable: with the increase in potential, the current density still remains close to zero, and it shows that, even in the presence of chloride ions, passivity remained under the tested conditions.

Alloy surfaces were investigated by scanning electron microscopy after the chronoamperometry measurements taken at the potential of 0.600 V. Fig. 15a–c presents FeCr alloy images where, (a) shows a surface well attacked by the presence of extensive pitting and (b) depicts the intergranular corrosion close to the alloy/resin interface. Detail 1 made it possible to better observe the intergranular corrosion in this material. This detail shows that pitting corrosion occurs in two distinct regions: inside the grain and on the grain boundary. In the boundary region, the process is more intense, and it is possible to see the coalescence of the pitting, which promotes the formation of discontinuous trenches, resulting in a pitting intergranular morphology. The nucleation and growth of pitting in the grain boundary region is also evident in Fig. 13c, obtained after the polarization tests. The formation of a pitting intergranular morphology was also observed by Ref. [76], who studied the mechanism of intergranular corrosion of AISI 304 and 304 L steels.

As discussed in section 3.2, globular precipitates were observed in the grain boundary region of the FeCr alloy (Fig. 4). The results of the thermodynamic simulation and the identification of these precipitates by SEM/EDS indicated that the main phase precipitated at the grain boundary of the FeCr alloy corresponds to the σ-phase. Based on the literature, σ phase can strongly affect the resistance to corrosion due to Cr impoverishment in the ferritic matrix, in adjacent regions to grain boundary [77]. The image in (c) shows the oxide aspect generated on material surface. One could notice the marks left by the surface sanding process, which suggested that the layer formed is not very thick.

Fig. 15d–f presents the surfaces of the FeCrY alloy. The general aspect of alloy surface was revealed in (d) and (e). The presence of pitting intergranular corrosion is clear, but it was not noticed after curve polarization (Fig. 13d–f). Several occurrences of micro-pitting were visualized in detail 2. Although pitting corrosion occurs mostly in the grain matrix, in Fig. 15d, it is clear that this form of corrosion also occurs in the grain boundary region. The coalescence of some pitting promotes the formation of a small ditch, in a process that would be related to the start of intergranular corrosion, which will possibly evolve into a typical ditch-like intergranular morphology.

According to the microstructural analysis of this alloy, in addition to the σ-phase, the $Fe_{17}Y_2$ and $Cr_{23}C_6$ phases were also found. All phases are located at the grain boundaries and could act to further weaken the material in terms of corrosion. However, both the polarization curves and the chronoamperometry tests show that the addition of Y increases the corrosion resistance of the FeCr alloy. Possible explanations for this behavior are the difference in morphology of the σ-phase and the formation of the $Fe_{17}Y_2$ precipitate.

In the grain boundary of the FeCrY alloy, the σ-phase has an elongated shape, unlike the globular precipitate observed in the grain boundary of the FeCr alloy, as shown in Fig. 4a and 5e. Villanueva et al. [44] and Chen and Yang [45]. relate the elongated shape to a less advanced stage of the σ-phase, so it is possible to consider that the addition of Y slows down the growth kinetics of this phase. Although the thermodynamic simulation did not predict the presence of Cr in the $F_{17}Y_2$ phase, the results of He et al. [49] state that at a temperature of 500.0 °C, up to 18 at. % of Cr can be reached in it, so it can be assumed that some percentage of Cr is found in its precipitates. It is therefore reasonable to propose that the presence of Cr in the $F_{17}Y_2$ phase would reduce the growth kinetics of the σ phase, which is deleterious to corrosion, thus justifying the greater corrosion resistance of the FeCrY alloy compared to FeCr.

It is important to observe that there are studies about ferrous alloys with 0.15% Y in the literature, which show the beneficial effect of this element for resistance to corrosion. According to Wang et al. [72], the addition of Y delays the precipitation of MnS inclusions, purifies the grain boundary and improves the alloy microstructure. According to these authors, this delay in MnS precipitation the region where pitting nucleates allows the emergence of yttrium sulphides or oxy-sulphides in its place; therefore, they increase the resistance to corrosion in this material.

Fig. 15g–i depict secondary electron images of the FeCrTi alloy. It is clear that surfaces were less attacked since there was no pitting at advanced stages or intergranular corrosion, due to the absence of the σ-phase in this alloy, as previously discussed. Regarding oxide morphology, it is important to highlight that the layer formed on the FeCrTi alloy is quite different from that observed in the FeCr and FeCrY alloys.

It is known that the favorite halogen adsorption sites are likely to be the regions presenting flaws in the oxide layers. These regions are featured by variations in film thickness; in this case, thinner regions in less uniform films show larger electric field through the oxide/solution interface, which easily attracts aggressive ions to this region. Thus, the adsorbed ions trigger a dissolution process in the oxide layer, which lasts until the passive film is locally dissolved and pitting nucleation takes place [77].

One can observe (Fig. 15i) that the FeCrTi alloy formed a thicker and more compact layer than that of the other alloys. Grooves generated during the polishing process were no longer observed. The morphology was also different, the layer was grainier and, apparently, more homogeneous. These aspects have certainly influenced the passivation ability of the FeCrTi alloy and have allowed a more effective protection against pitting and intergranular corrosion in the material.

3.3.3. Electrochemical impedance

Fig. 16a–c present the Nyquist diagram and Bode representations adjusted for the electrolyte resistance. The impedance spectra were taken at open-circuit potential and adjustments in phase angle and in the impedance modulus were carried out through equations (1) and (2), respectively [78].

$$\phi_{adj} = tan^{-1} \qquad \text{Equation 1}$$

$$|Z|_{adj} = \sqrt{\left(Z' - R_{e,est}\right)^2 +} \qquad \text{Equation 2}$$

Based on the Nyquist diagram (Fig. 16a), all materials presented semi-opened and flattened plane capacitive arcs. This non-ideal behavior is typical of solid electrodes and, most of the time, it is related to frequency dispersion, which emerges because of roughness and of other surface heterogeneities [79]. According to Gharbi et al. [78], this diagram profile is in compliance with the capacitive response that is often observed in oxide films on electrode surface.

Fig. 16a shows that the materials were divided into two groups: AISI 430 and the FeCrY alloy presented quite similar behaviors, they recorded the lowest impedance values, whereas AISI 304 and the FeCr and FeCrTi alloys presented the highest impedance values. Based on the impedance module shown in Fig. 16b, it is not possible to observe significant difference between materials as seen in the Nyquist representation. On the other hand, a clearer response was observed through the phase angle shown in Fig. 16c.

Phase angle values are lower in AISI 430 (−72°) and in the FeCrY alloy (−76°), while the other alloys show phase angles close to −80°. This result corroborated the behavior observed in the Nyquist diagrams, which suggest that a less resistive film is formed on the materials with

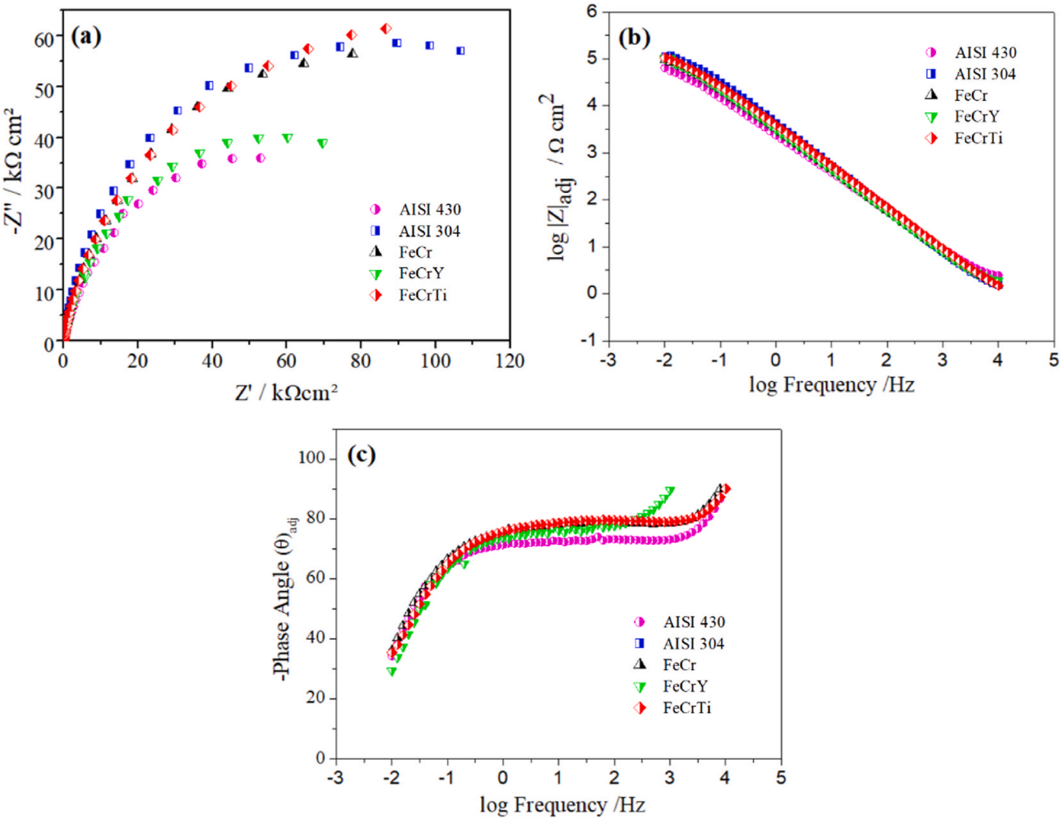

Fig. 16. Impedance data at potential of corrosion applied to commercial steel and to the Fe–Cr-X alloys in a 3.5 wt% NaCl solution without agitation and at RT; (a) Tradition Nyquist representation (b) Bode representation of the impedance modules corrected based on the ohmic resistance (c) Bode representation of the phase angle corrected based on the ohmic resistance.

the smaller phase angles. The broad plateau of maximum was another factor observed. This behavior suggests that events presenting different time constants take place in the double electric layer. These events can be related to high impedance in the passive area of the oxide layer, in comparison to the lower impedance resulting from flaws in these layers, such as the presence of pitting [80]. There was phase angle increase in the high frequency region in all materials. According to Hirschorn et al. [81], such an increase is attributed to a normal time constant distribution caused by variations in resistivity within the oxide film.

Constant Phase elements (CPEs) are commonly used in the analysis of experimental impedance data to account for the non-ideal behavior of capacitive elements. The CPE elements $(\alpha \wedge Q_{eff})$ were determined in accordance with Orazem et al. [78]. The value of α was determined from the curve inclination in the high-frequency region, as shown in Fig. 17. When $\alpha \neq 1$, the system shows the behavior that has been attributed to surface heterogeneity or to the continuously distributed time constants for charge-transfer reactions [82]. The coefficient values recorded for α allowed determining the effective coefficient of CPE Q_{eff}, based on equation (3) [81,83].

$$Q_{eff} = \sin(\alpha\pi / 2\,)1 / z''(f)(2\pi f) \qquad \text{Equation 3}$$

According to Hirschorn et al. [81] and Brug et al. [83] it is possible to calculate effective capacitance values based on CPE parameters.

However, the assessment of C_{eff} is based on the values of R_e (ohmic resistance) and Rt (charge transfer resistance). In view of the experimental data obtained in this work, due to the nature of the passive layer in the alloys evaluated, the Nyquist diagrams show open arcs. Thus, extrapolating the capacitive arc in the low frequency region implies reasonable errors. However, some studies have used Q_{eff} as a reasonable estimate to express the system's capacitance [78,79]. Therefore, in this study, the C_{eff} values were not assessed and the Q_{eff} values were used as an estimate of the system capacitance. The α and $Q_{eff,}$ values are shown in Table 9.

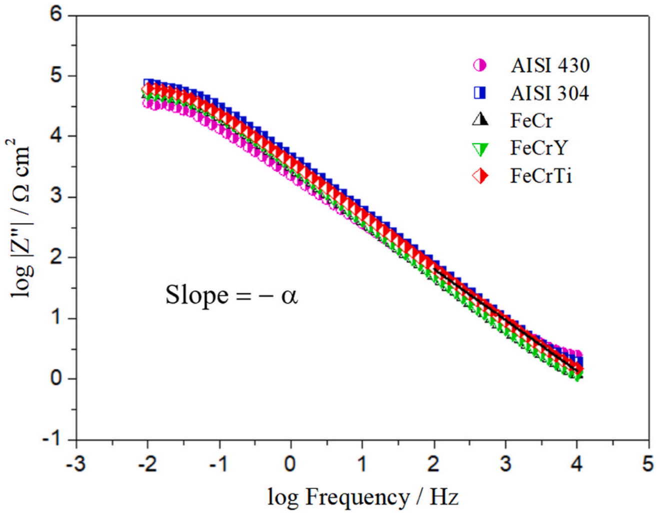

Fig. 17. Imaginary part of impedance as function of frequency for commercial steels and Fe–Cr-X alloys in OCP in 3.5 wt% NaCl solution without agitation and at RT. The line with slope -α fitted the high frequency.

According to the results, the values of α and Q_{eff} are close for the alloys AISI 304 and FeCrTi. Regarding the other alloys produced for this study, the FeCr alloy has Q_{eff} lower than that of the FeCrY alloy. The polarization curve (Fig. 12) showed that the FeCr and FeCrY alloys have similar profiles, although the presence of Y caused great stability in the currents, especially at low polarizations. Above approximately +0.220

Table 9
CPE parameters for experimental impedance data obtained in the OCP, *versus* Ag/AgCl reference electrode.

Alloys	α	Q_{eff} ($\times 10^{-4}$ $\Omega^{-1}cm^{-2}s^{\alpha}$)
AISI 430	0.736	2.113
AISI 304	0.837	0.653
FeCr	0.828	0.935
FeCrY	0.765	1.386
FeCrTi	0.840	0.667

V, the currents remain lower than those observed for the FeCr alloy until the end of the test.

With the objective of better understanding the behavior of elements Ti and Y in the alloys produced for this research, electrochemical impedance assays were carried out outside the OCP. The chosen potential of 0.600 V *versus* Ag/AgCl reference electrode corresponds to the region close to the E_b of the FeCrTi alloy. Fig. 18a–c presents the Nyquist diagrams and the Bode representations of the FeCr, FeCrY and FeCrTi alloys. Now it is easy to observe the distinction between the behaviors of these alloys. Fig. 18a shows one capacitive arc in the high- and mid-frequency region and one inductive arc with great dispersion in the low frequency region for all alloys.

Inductive arcs are related to effective dissolution of the alloys at this potential [84–86]. It was also possible to observe that the capacitive arcs, previously noted in the measurements in OCP, had significantly decreased in size. This outcome pointed out to the evolution of corrosive processes on the surfaces of the alloys. However, this condition not only allowed the beneficial effect of Ti to be reaffirmed, but also revealed more clearly that Y also contributes to improving the corrosion resistance of the FeCr alloy, corroborating with the chronoamperometry.

By analyzing the Bode representations shown in Fig. 18b–c, one can extract interesting information about the oxide layers. The impedance module representation evidences that the linear region at median frequencies reduced significantly at a potential of 0.600 V and there was great dispersion associated with a new time constant in the low-frequency region. This behavior depicts an important reduction in the alloy capacitive profile, which is also reflected on the corrected phase angles. The broad plateau of maximum observed in OCP fully disappeared under this condition and a significant reduction in the values of the angles was also observed.

The α and Q_{eff}, values obtained at the potential at 0.600 V are shown in Table 10. The Q_{eff} values show a reduction in the capacitive behavior of the oxide layers as expected. Fig. 19a–b shows the behavior of Q_{eff} as a function of frequency for data obtained in OCP and at a potential of 0.600 V. Regarding OCP, Q_{eff} showed that oxides formed on the AISI 304

Table 10
CPE parameters applied to impedance data collected at potential of 0.600 V *versus* Ag/AgCl reference electrode.

Alloy	α	Q_{eff} ($\times 10^{-4}$ $\Omega^{-1}cm^{-2}s^{\alpha}$)
FeCr	0.463	14.78
FeCrY	0.532	6.312
FeCrTi	0.794	0.618

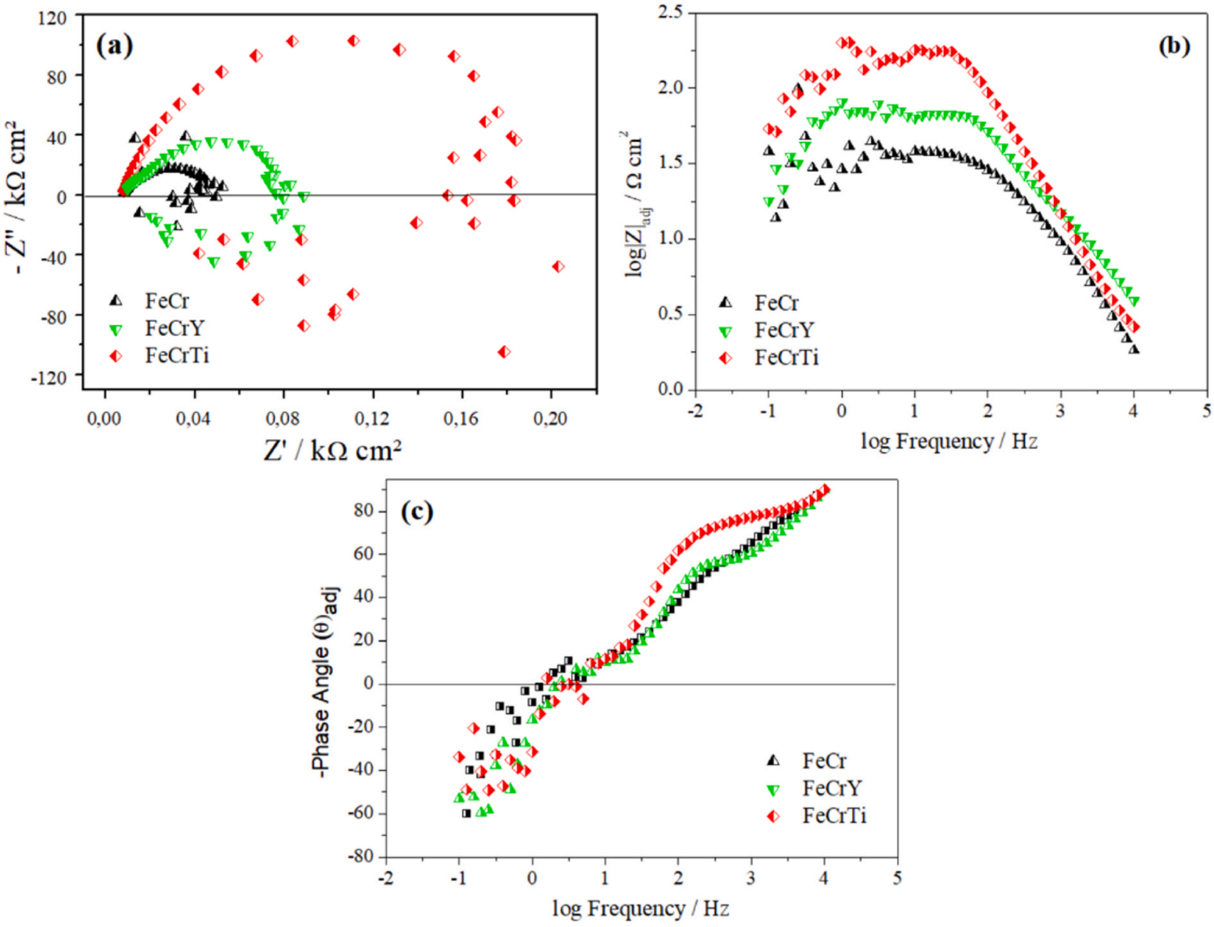

Fig. 18. Impedance data at potential of 0.600 V applied to Fe–Cr-X alloys in 3.5 wt% NaCl solution without agitation and at RT; (a) Tradition Nyquist representation (b) Bode representation of the impedance modules corrected based on the ohmic resistance (c) Bode representation of the phase angle corrected based on the ohmic resistance.

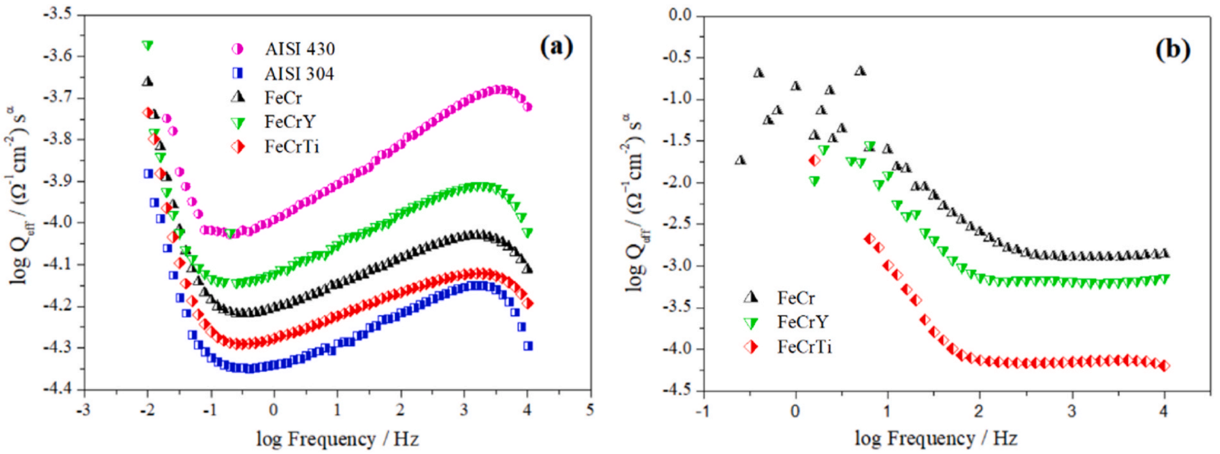

Fig. 19. Effective CPE Coefficient defined through Eq. (6): (a) commercial steels and Fe–Cr-X alloys in OCP; (b) Fe–Cr-X alloys at potential of 0.600 V.

and the FeCrTi alloy presented a more capacitive behavior than the others. The worst performance was attributed to AISI 430 and the FeCr and FeCrY alloys recorded intermediate behavior. Regarding potential of 0.600 V, where only the alloys produced for this study were evaluated, Fig. 19b shows that the capacitive performance increased in the following order FeCrTi, FeCrY and FeCr. This behavior is in agreement

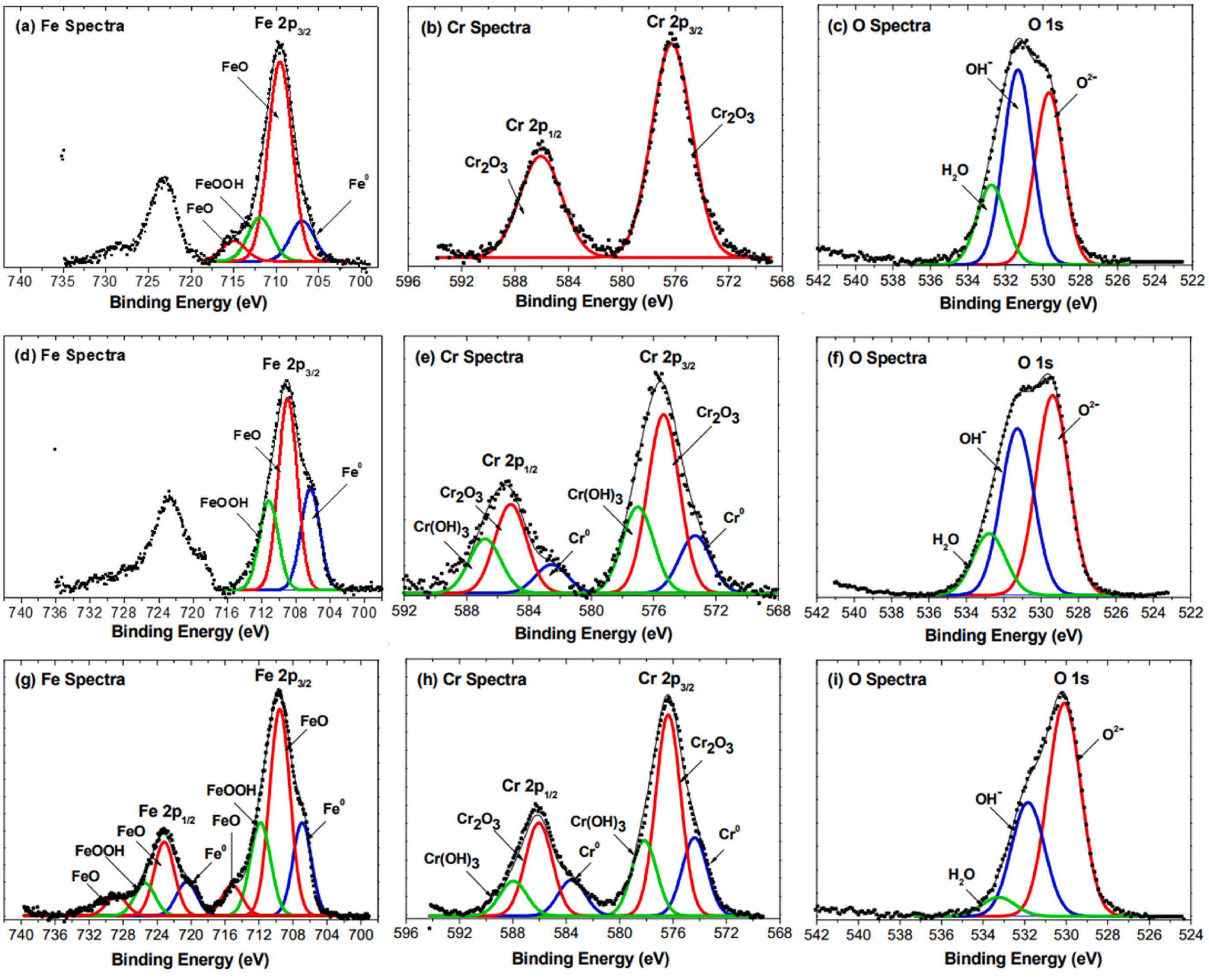

Fig. 20. XPS spectra of Fe 2p, Cr 2p and O 1s of the films formed on FeCr (a–c), FeCrY (d–f) and FeCrTi (g–i) alloys after chronoamperometry tests at 0.100 V for 3600s in 3.5 wt % NaCl solution without agitation and at RT.

with the polarization curves and chronoamperometry results.

3.3.4. X-ray Photoelectron Spectroscopy

The XPS analysis was used to determine the compositions of the passive films on Fe–Cr-X alloys in 3.5% NaCl solution. Fig. 20 shows Fe 2p, Cr 2p and O 1s XPS spectra of the films formed in potential of 0.100 V maintained by 3600s on FeCr (a-c), FeCrY (d-f) and FeCrTi (g-i) alloys. From this figure, it can be seen that the Fe 2p spectrum is mainly composed of FeO, FeOOH and Fe, whereas Cr_2O_3, $Cr(OH)_3$ and Cr are found in Cr 2p spectrum, except for FeCr alloy, which indicates only the existence of Cr_2O_3. The O 1s spectrum, in its turn, was deconvoluted into three peaks, which were attributed to metallic oxides (FeO and Cr_2O_3), oxyhydroxides and hydroxides (FeOOH and $Cr(OH)_3$), and adsorbed H_2O. Considering the three alloys, it can be said that these results are quite consistent with saline media [87,88].

As previously stated, all alloys in this study have high Cr content and this element is the main driving force for improving the stability and corrosion resistance due to Cr_2O_3 formation. It is also a fact that the addition of Y and Ti to FeCr alloys has enhanced their corrosion behavior, especially the latter, as shown by the electrochemical tests (Figs. 12, 14, 16 and 18), but no compounds related to such elements were observed in the passive films, indicating an indirect contribution.

Before going into this analysis, it is first worth considering the role of the identified components. In this regard, it is seen in the literature that FeOOH, formed on all Fe–Cr-X alloys, contributes to the improvement of metal-medium interfaces, since it can block part of corrosive ions from entering [87,89]. Therefore, a FeOOH-enriched passive film could improve the corrosion resistance of Fe–Cr alloys immersed in NaCl solution. In contrast, for $Cr(OH)_3$, not identified only in the FeCr alloy, it is observed to have little influence on this medium [90], although it shows positive effects in CO_2-rich environments.

As for FeO, Ramya et al. [91] observed that its interaction with Cr_2O_3 leads to the formation of $FeCr_2O_4$ at the initial stages of pitting. For Wang et al. [87], the oxidation of Cr into Cr_2O_3 and its subsequent binding with FeO to form the $FeCr_2O_4$ is beneficial, since the metal medium interface transforms from the corrosion products to the passive film, improving the compactness of Cr_2O_3. This reaction normally takes place as the Cr content further increased to 18 wt%. On the other hand, the excessive Cr (40 wt%) promotes the formation of $FeCr_2O_4$ instead of Cr_2O_3, which results in a decline of the corrosion resistance. Therefore, the presence of FeO in passive films of FeCr, FeCrY and FeCrTi alloys is encouraging, since this component plays a supporting role against chloride ion attack.

In addition to these compounds, the existence of the metallic states in the passive films (Cr^0 and Fe^0 for the FeCrY and FeCrTi alloys, and Fe^0 for the FeCr alloy) is clearly observed. According to Wang et al. [92], the metallic states may exist in this condition, especially in the inner film. When these are present in the topmost surface, they may come from the transformation from the corrosion products to the passive film [88]. Thus, it is evident that all alloys present very similar characteristics regarding the nature of their layers, which are consistent with the properties presented. However, Fig. 20 alone does not elucidate the differences found in the electrochemical tests. The atomic compositions of the elements present in the passive films, seen in Table 11, seem to guide the understanding of this issue.

From Table 11, one can see that the concentration of Fe is higher than that of Cr in all alloys as a consequence of its high content in the bulk and high mobility through the film [92]. It is also noted that the FeCrTi alloy showed the highest concentrations of Fe and Cr atoms when compared to the other compositions, being this alloy the one that presented the best corrosion resistance, according to the anodic polarization curves (Fig. 12) and chronoamperometric curves (Fig. 14) and impedance data (Figs. 16 and 18). In this case, it is worth noting that the increase in Fe concentration is quite expressive and may be a consequence of the increase in Cr concentration itself.

Table 11
Atomic compositions of passive films formed on FeCr, FeCrY and FeCrTi alloys after chronoamperometry test at 0.100 V for 3600s in NaCl solution.

Alloy	Relative atomic concentration (at.%)		
	Fe	Cr	O
FeCr	10	6	Balance
FeCrY	10	6	Balance
FeCrTi	18	8	Balance

According to Wang *et al.* [87], increasing Cr content promotes the dissolution and oxidation of Fe, which further contributes to the formation of FeOOH. This can lead to a more compact FeOOH outer layer, which prevents oxygen diffusion and improves the corrosion protection properties of the metal-medium interface [89]. Moreover, when the Cr concentration increases, more effective is the protection against corrosion [93]. In this case, it is likely that in the FeCrTi alloy, the Cr_2O_3 content is higher and that the enrichment of both Cr_2O_3 and FeOOH is providing a more stable and more corrosion resistant passive film, similarly to that was observed by Wang et al. [87], who investigated the effect of the addition of Cr to Fe–Cr alloys in 3.5 wt% NaCl solution.

Since a higher concentration of Cr provides benefits and its concentration is the same in the three alloys (close to 25 wt%), then its increase in the passive film formed on the FeCrTi alloy can only have been stimulated by the addition of Ti. In this respect, it is seen that the minor alloying elements can form a solid solution with the major element and once the passive film is formed, these are incorporated into its lattice as dopants, modifying its properties [94,95]. Here, it is important to highlight that in the FeCrTi alloy, it was observed that the Fe lattice parameter increased because of the dissolution of Ti atoms in the Fe-based solid solution (Fig. 3). It is a fact that Cr itself is an alloying element that is also in solid solution with Fe, which has a relatively high content in these alloys, and it is essential for good corrosion resistance, but attention must be paid at this point to the minority alloying element.

Generally, a passive film presents a bilayer structure consisting of oxides growing from the metal, and an outer one composed of precipitated hydroxide or oxyhydroxide, where the alloying elements from the substrate alloy may be incorporated in both layers [95,96]. In this study, the passive films can be said to have an inner layer mainly composed of Cr_2O_3 and FeO, and an outer layer of $Cr(OH)_3$ and FeOOH.

According to Jiang et al. [94], the presence of dopants significantly affects or even controls the concentrations of the defects in an oxide layer. This information allows us to understand the relative importance of small additions of alloying elements on the formation of defects that could be responsible for ion transport in a passive layer. Thus, considering the works of Atkinson et al. [97] and Blacklocks et al. [98], the solubility of Ti ions into the main Cr_2O_3 lattice on the FeCrTi alloy will produce complex defects of lower energy, where the Ti is predominantly present as Ti^{4+} in a Cr^{3+} site, whose dominant defects are Ti^{4+} ions charge-compensated by Cr^{3+} vacancies. The presence of a thicker passive layer in the FeCrTi alloy, as already discussed in Fig. 20i, is consistent with these studies that point to increased imperfections in the oxide lattice, which leads to an increase in the mass transport of ions [94]. It is also seen that a passive film enriched with FeO and Cr_2O_3 typically exhibits p-type semiconductivity due to cation vacancies [99], which leads to the understanding that an analogous mechanism may be observed in the case of FeO. For the FeCrY alloy, it should be pointed out that no solubility of Y was observed in the α-Fe lattice. Furthermore, Hagel and Seybolt [100] state that the doping of α-Cr_2O_3 with Y_2O_3 has very little effect on cation diffusion rates, since for Y^{3+} ions no charge compensation is required.

For a complete understanding of the corrosion behavior of these alloys, it is important to go over some information about their microstructures. In this sense, the FeCrTi alloy also has a more favorable microstructure, since it presented titanium carbonitrides and possibly TiC, which favor corrosion resistance [59]. The FeCrY alloy, in its turn, presented a microstructure with the presence of a few elongated σ particles, together with the $Fe_{17}Y_2$ phase at the grain boundaries, as well as the formation of $Cr_{23}C_6$ and Y_2O_3. This configuration has a lower impact on corrosion resistance when compared to the FeCr alloy, which showed the formation of larger σ particles with a globular morphology, and the precipitation of $Cr_{23}C_6$, which contributes to causing Cr depletion in the adjacent matrix. Therefore, these results show that the addition of 0.18 wt % Ti to the FeCr alloy brought several benefits, both in microstructural aspects, which remove the possibility of some type of localized corrosion, and in its indirect action into the oxide layer, increasing the concentrations of Cr and Fe, what may have led to the enrichment of both Cr_2O_3 and FeOOH, thus producing a passive film more stable and resistant to attack by chloride ions.

4. Conclusions

In this study, the influence of Y and Ti additions on the microstructure and corrosion resistance of the FeCr alloy was investigated and the results led to the following conclusions:

(a) The volume fractions of the precipitated phases are very low ($<10^{-2}$) for all alloys, with the exception of the σ-phase, which reaches ~0.14 at 600 °C, according to equilibrium phase calculations;
(b) The microstructures of the FeCr, FeCrY and FeCrTi alloys presented an α-Fe matrix with coarse grains having average values of 137.8 ± 61.9, 113.9 ± 61.4 and 130.9 ± 70.7 μm, respectively, which shows that the additions (~0.2 wt%) of Y and Ti were not enough to trigger adequate refinement;
(c) The FeCr alloy showed low σ-phase precipitation on the grain boundary with a globular appearance, as well as the formation of $Cr_{23}C_6$, which leads to Cr depletion in the adjacent matrix;
(d) The FeCrY alloy presented precipitation of a Y-rich phase, identified as $Fe_{17}Y_2$, which was accompanied by an elongated σ-phase, both located at the grain boundaries. Other precipitates such as $Cr_{23}C_6$ and Y_2O_3 were also observed, showing that this alloy has a quite heterogeneous microstructure;
(e) The FeCrTi alloy presented Ti(C,N) precipitates dispersed within the α-Fe matrix, and a nanometric precipitation of Ti rich particles, which were attributed to the formation of TiC. The absence of precipitation of the σ phase in this alloy shows that the addition of 0.18 wt % of Ti was able to inhibit its formation;
(f) The electrochemical tests showed that the alloys produced for this study were more resistant to corrosion than commercial stainless steels, since the oxides formed are more resistive, a fact proven by the lower current density values and lower Q_{eff} obtained in these samples.
(g) The best performance of the FeCrTi alloy was attributed to the inhibition of σ-phase, as well as to the formation of a more compact, homogeneous and resistive oxide layer capable of reducing the possibility of galvanic microcell formation;
(h) Although pitting corrosion has been observed both in the matrix and at the grain boundaries in FeCr and FeCrY alloys, the presence of Y delayed the formation of the σ phase and improved the corrosion resistance of the alloy;
(i) Impedance experimental data assessed based on constant phase elements showed that the highest α value was recorded for the FeCrTi alloy, which is indicative of the more capacitive behavior of this material than that of the other alloys. This behavior was confirmed through Q_{eff} in the entire frequency range used. The most capacitive profile recorded for the FeCrTi alloy was also observed at a potential of 0.600 V. This behavior corroborates results presented in the chronoamperometry, which confirmed that Ti addition increased the resistance to corrosion of the FeCr alloy;
(j) The passive films formed on Fe–Cr-X alloys contain Cr_2O_3, FeO, $Cr(OH)_3$ (except for the FeCr alloy) and FeOOH, as demonstrated by X-ray photoelectron spectra. For the FeCrTi alloy, Ti acted indirectly on the oxide layer, increasing the concentrations of Cr and Fe, which may have caused an enrichment of Cr_2O_3 and FeOOH, thus enhancing the protective characteristics of the passive film.

Declaration of competing interest

The authors declare that they have no known competing financial interests or personal relationships that could have appeared to influence the work reported in this paper.

Acknowledgements

The authors acknowledge the financial support from the Brazilian research agency CAPES and the support from UFS, through the use of the facilities of the Multiuser Laboratories of the Department of Materials Science and Engineering (CLMDCEM) and of the Laboratory of Microstructures and Mechanical Properties (LAMP).

References

[1] Lo KH, Shek CH, Lai JKL. Recent developments in stainless steels. Mat. Sci. Eng. R 2009;65:39–104. https://doi.org/10.1016/j.mser.2009.03.001.
[2] Zhang S, Li H, Jiang Z, Zhang B, Li Z, Wu J, Fan S, Feng H, Zhu H. Effects of Cr and Moon precipitation behavior and associated intergranular corrosion susceptibility of superaustenitic stainless steel S32654. Mater. Charact 2019;152: 141–50. https://doi.org/10.1016/j.matchar.2019.04.010.
[3] Lee C, Roh S, Lee C, Hong S. Influence of Si on sigma phase precipitation and pitting corrosion in superaustenitic stainless steel weld metal. Mater Chem Phys 2018;207:91–7. https://doi.org/10.1016/j.matchemphys.2017.12.055.
[4] Rajkumar M, Babu SPK, Nagaraj TA. Intergranular corrosion characteristics of niobium stabilized 27Cr-7Ni-Mo-W-N cast hyper duplex stainless steel. Mater Today-Proc 2020;27:2551–5. https://doi.org/10.1016/j.matpr.2019.10.134.
[5] Kang Y, Mao WM, Chen YJ, Jing J, Cheng M. Effect of Ti content on grain size and mechanical properties of UNS S44100 ferritic stainless steel. Mat. Sci. Eng. A 2016;677:211–21. https://doi.org/10.1016/j.msea.2016.08.070.
[6] Mallaiah G, Reddy PR, Kumar A. Influence of titanium addition on mechanical properties, residual stresses and corrosion behavior of AISI 430 grade ferritic stainless steel GTA welds. Procedia Mater. Sci2 2014:1740–51. https://doi.org/10.1016/j.mspro.2014.07.204.
[7] Blachowski A, Cieslak J, Dubiel SM, Sepiol B. Effect of titanium on the kinetics of the σ – phase formation in a coarse-grained Fe-Cr alloy. Intermetallics 2000;8: 963–6. https://doi.org/10.1016/S0966-9795(00)00026-1.
[8] Blachowski A, Cieslak J, Dubiel SM, Zukrowski J. Effect of titanium on the kinetics of the σ – phase formation in a small grain Fe-Cr alloy. J. Alloy Compd. 2000;308:189–92. https://doi.org/10.1016/S0925-8388(00)00835-5.
[9] Vander Voort GF, Lucas GM, Manilova EP. Metallography and microstructures of heat-resistant alloys. ASM Handbook: Metallography and microstructure 2004;9: 820–59. Materials Park, Ohio.
[10] Xue W, Li Z, Xiao K, Yu W, Song J, Chen J, Dong C, Li X. Initial microzonal corrosion mechanism of inclusions associated with the precipitated (Ti, Nb)N phase of Sb-containing weathering steel. Corros. Sci. 2020;163:108232. https://doi.org/10.1016/j.corsci.2019. 108232.
[11] Azevedo ACRF, Padilha AF. The most frequent failure causes in super ferritic stainless steels: Are they really super? Procedia Structural Integrity 2019;17: 331–8. https://doi.org/10.1016/j.prostr.2019.08.044.
[12] Wan B, Chen W, Liu L, Cao X, Zhou L, Fu Z. Effect of trace yttrium addition on the microstructure and tensile properties of recycled Al-7Si-0.3Mg-1.0Fe e casting alloys. Mater. Sci. Eng. A 2016;666:165–75. https://doi.org/10.1016/j.msea.2016.04.036.
[13] Li XI, He SM, Zhou XT, Zou Y, Li ZJ, Li AG, Yu XH. Effects of rare earth yttrium on microstructure and properties of Ni-16Mo-7Cr-4Fe nickel-based superalloy. Mater. Charact. 2014;95:171–9. https://doi.org/10.1016/j.matchar.2014.06.016.
[14] Su J, Guo F, Cai H, Liu L. Study on alloying element distribution and compound structure of AZ61 magnesium alloy with yttrium. J Phys Chem Solid 2019;131: 125–30. https://doi.org/10.1016/j.jpcs.2019.03.021.
[15] Woo SK, Blawert C, Yasakau KA, Yi S, Scharnagl N, Suh B-C, Kim YM, You BS, Yim CD. Effects of combined addition of Ca and Y on the corrosion behaviours of die-cast AZ91D magnesium alloy. Corros. Sci. 2020;166:108451. https://doi.org/10.1016/j.corsci.2020.108451.
[16] Wang MF, Xiao DH, Zhou PF, Liu WS, Ma YZ, Sun BR. Effects of rare Earth yttrium on microstructure and properties of Mg-Al-Zn alloy. J. Alloy Compd. 2018;742: 232–9. https://doi.org/10.1016/j.jallcom.2018.01.234.
[17] Xu X, Wei H, Xiang J, Wang L, Liu M, Zhang H, Men D, An J. Oxidation mechanism of three Fe-Al alloys with and without addition of 0.1 at% Y at 800 °C. J Rare Earths 2020;38:1126–30. https://doi.org/10.1016/j.jre.2019.10.007.

[18] Pandey JL, Prakash S, Mehta ML. Effects of varying the zirconium concentration and 1 wt.% Y on high temperature oxidation of Fe-15wt.%Cr-4wt.%Al alloy under isothermal and cyclic conditions. J Less Common Met 1990;159:23–34. https://doi.org/10.1016/0022-5088(90)90128-7.

[19] Hsieh C-C, Lin D-Y, Wu W. Precipitation behavior of σ phase in 19Cr–9Ni–2Mn and 18Cr–0.75Si stainless steels hot-rolled at 800°C with various reduction ratios. Mater. Sci. Eng. A 2007;467:181–9. https://doi.org/10.1016/j.msea.2007.02.107.

[20] Zheng H, Ye XN, Li JD, Jiang LZ, Liu ZY, Wang GD, Wang BS. Effect of carbon content on microstructure and mechanical properties of hot-rolled low carbon 12Cr–Ni stainless steel. Materials Science and Engineering: A 2010;527(27–28): 7407–12. https://doi.org/10.1016/j.msea.2010.08.023.

[21] American Society for Testing and Materials – ASTM. ASTM a240/a240m-23a: standard specification for chromium and chromium-nickel stainless steel plate, sheet, and strip for pressure vessels and for general applications. West Conshohocken: ASTM International; 2023. https://cdn.standards.iteh.ai/samples/116530/cfeccb22b8d546b7b6f246a9fc69574c/ASTM-A240-A240M-23a.pdf.

[22] Park I-S, Chan Jung Y, Seong S, Ahn J, Kang J, Noh W, Lansalot-Matras C. Atomic layer deposition of Y_2O_3 films using heteroleptic liquid $(iPrCp)_2Y(iPr\text{-}amd)$ precursor. J Mater Chem C 2014;2:9240–7. https://doi.org/10.1039/c4tc01405g.

[23] Pourbaix M. Atlas of electrochemical equilibria in aqueous solutions. 2 ed. NACE International Cebelcor; 1974.

[24] Kim SI, Yoo YC. Continuous dynamic recrystallization of AISI 430 ferritic stainless steel. Met Mater Int 2002;8:7–13. https://doi.org/10.1007/BF03027023.

[25] Mehtonen S, Karjalainen LP, Porter DA. Effect of hot deformation temperature on the restoration mechanisms and texture in a high-Cr ferritic stainless steel. Mater Sci Forum 2013;762:705–10. https://10.4028/www.scientific.net/MSF.762.705.

[26] Braga FV, Escobar DP, de Oliveira NJL, Andrade MS. Hot deformation behavior of a ferritic stainless steel stabilized with Nb during hot rolling simulation at different temperature ranges. J Mater Res 2016;31:635–45. https://doi.org/10.1557/jmr.2016.57.

[27] Zhou Lh, Bi Hy, Sui Fl, Du W, Fang Xs. Influence of finish rolling temperature on microstructure and properties of hot-rolled SUS436L stainless steel. J Mater Eng Perform 2023;32:8441–51. https://doi.org/10.1007/s11665-022-07719-y.

[28] Han J, Zhu Z, Wei G, Jiang X, Wang Q, Cai Y, Jiang Z. Microstructure and mechanical properties of Nb- and Nb + Ti-stabilised 18Cr–2Mo ferritic stainless steels. Acta Metall Sin (Engl Lett) 2020;33:716–30. https://doi.org/10.1007/s40195-019-00988-y.

[29] Li J, Xiao X, Yuan C, Gao X, Bao X. Effect of yttrium on the mechanical and magnetostrictive properties of $Fe_{83}Ga_{17}$ alloy. J Rare Earths 2015;33:1087–92. https://doi.org/10.1016/S1002-0721(14)60530-5.

[30] Ke Y, Duan H, Sun Y. Effect of yttrium and erbium on the microstructure and mechanical properties of Ti–Al–Nb alloys. Mat Sci. Eng. 2010;A528:220–5. https://doi.org/10.1016/j.msea.2010.09.011.

[31] Li Q, Yang Z, Xia C, Wang X, Yang T, Liang C, Yin F, Liu R. Effects of Y addition on microstructure and mechanical properties of Ti-25Zr alloys. Mat Sci. Eng. 2019; A748:236–43. https://doi.org/10.1016/j.msea.2019.01.096.

[32] Cui C, Wu L, Wu R, Zhang J, Zhang M. Influence of Yttrium on microstructure and mechanical properties of as-cast Mg-5Li-3Al-2Zn alloy. J Alloy Compd 2011;509: 9045–9. https://doi.org/10.1016/j.jallcom.2011.04.030.

[33] Shan Y, Luo X, Hu X, Liu S. Mechanisms of solidification structure improvement of ultra pure17 wt.% Cr ferritic stainless steel by Ti, Nb addition. J Mater Sci Technol 2011;27:352–8. https://doi.org/10.1016/S1005-0302(11)60073-X.

[34] Michelic SK, Loder D, Reip T, Ardehali Barani A, Bernhard C. Characterization of TiN, TiC and Ti(C,N) in titanium-alloyed ferritic chromium steels focusing on the significance of different particle morphologies. Mater. Charact. 2015;100:61–7. https://doi.org/10.1016/j.matchar.2014.12.014.

[35] Shi C, Cheng G, Li Z, Zhao P. Solidification structure refining of 430 ferrite stainless steel with TiN nucleation. J Iron Steel Res Int 2008;15:57–60. https://doi.org/10.1016/S1006-706X(08)60126-0.

[36] Kang Y, Mao WM, Chen YJ, Jing J, Cheng M. Effect of Ti content on grain size and mechanical properties of UNS S44100 ferritic stainless steel. Mat Sci. Eng. A 2016;677:211–21. https://doi.org/10.1016/j.msea.2016.08.070.

[37] Cullity BD. Elements of X-ray diffraction. Nabu Press; 2011.

[38] Biezma MV, Martin U, Linhardt P, Ress J, Rodríguez C, Bastidas DM. Non-destructive techniques for the detection of sigma phase in duplex stainless steel: a comprehensive review. Eng Fail Anal 2021;122:105227. https://doi.org/10.1016/j.engfailanal.2021.10.

[39] Harmer CP, Kamali S, Lebedev OI, Lee SJ, Ribeiro RA, Canfield PC, Kovnir K. Pseudo-polymorphism in layered FeS intercalates: a competition between charged and neutral guest species. Chem Mater 2022;34:5397–408. https://doi.org/10.1021/acs.chemmater.2c00270.

[40] Machida A, Saitoh H, Hattori T, Sano-Furukawa A, i Funakoshi K, Sato T, Orimo S-i, Aoki K. Hexagonal close-packed iron hydride behind the conventional phase diagram. Sci Rep 2019;9:12290. https://doi.org/10.1038/s41598-019-48817-7.

[41] Saenko I, Fabrichnaya O, Udovsky A. New thermodynamic assessment of the Fe-Y system. J. Phase Equilib. Diffus 2017;38:684–99. https://doi.org/10.1007/s11669-017-0574-3.

[42] Gao X, Ren H, Wang H, Chen S. Activity coefficient and solubility of yttrium in Fe-Y dilute solid solution. J Rare Earths 2016;34:1168–72. https://doi.org/10.1016/S1002-0721(16)60149-7.

[43] Muthaiah VMS, Babu LH, Koch CC, Mula S. Feasibility of formation of nanocrystalline Fe-Cr-Y alloys: mechanical properties and thermal stability. Mater. Charact. 2016;114:43–53. https://doi.org/10.1016/j.matchar.2016.02.005.

[44] Villanueva DME, Junior FCP, Plaut RL, Padilha AF. Comparative study on sigma phase precipitation of three types of stainless steels: austenitic, superferritic and duplex. J Mater Sci Technol 2006;22:1098–104. https://doi.org/10.1179/174328406X109230.

[45] Chen TH, Yang JR. Effects of solution treatment and continuous cooling on σ-phase precipitation in a 2205 duplex stainless steel. Mater. Sci. Eng. 2001;A311: 28–41. https://doi.org/10.1016/S0921-5093(01)00911-X.

[46] Cardoso PHS, Kwietniewski C, Porto JP, Reguly A, Strohaecker TR. The influence of delta ferrite in the AISI 416 stainless steel hot workability. Mat Sci. Eng. A 2003;351:1–8. https://doi.org/10.1016/S0921-5093(01)01740-3.

[47] Schwaab P. Duplex steels. Part II: carbides and nitrides. Metallogr. Microstruct. Anal 2013;2:343–51. https://doi.org/10.1007/s13632-013-0088-2. Proceedings of the Conference on Progress in Metallography (Special Editions of Practical Metallography)14 (1983) 435–444. apud M.Knyazeva and M. Polh.

[48] Wang C, Pan J, Yang Z, Lin J, Cao P, Su C, Li C, Yao M, Xiao X. Yttrium effect on 475 °C brittleness of Fe–13Cr–6Al–2Mo-0.5Nb-0.15Zr alloy. J Mater Res Technol 2024;29:5681–92. https://doi.org/10.1016/j.jmrt.2024.03.051.

[49] He W, Wang X, He J, Wen J, Yu M, Zeng L. Isothermal section of the Y–Fe–Cr ternary system at 773K. J Alloy Compd 2010;502:87–91. https://doi.org/10.1016/j.jallcom.2010.04.161.

[50] W R, Chalmers B. The segregation of impurities to grain boundaries. Acta Metall 1955;3:17–21. https://doi.org/10.1016/0001-6160(55)90005-5.

[51] Watanabe T, Kitamura S, Karashima S. Grain boundary hardening and segregation in alpha Iron-Tin alloy. Acta Metall 1980;28:455–63. https://doi.org/10.1016/0001-6160(80)90135-2.

[52] Raabe D, Ponge D, Kirchheim R, Assadi H, Li Y, Goto S, Kostka A, Herbig M, Sandlöbes S, Kuzmina M, Millan J, Yuan L, Choi P-P. Interface segregation in advanced steels studied at the atomic scale. In: Molodov DA, editor. Microstructural design of advanced engineering materials. Wiley-VCH Verlag GmbH & Co. KgaA; 2013. p. 267–98. https://doi.org/10.1002/9783527652815.ch11.

[53] Zhuang Y, Zhang X, Peng T, Fan H, Zhang X, Yan Q, Volinsky AA. Effects of yttrium oxides on the microstructure and mechanical properties of 15-15Ti ODS alloy fabricated by casting. Mater Char 2020;162:110228. https://doi.org/10.1016/j.matchar.2020.11022.

[54] Humphreys FJ, Miller WS, Djazeb MR. Microstructural development during thermomechanical processing of particulate metal-matrix composites. Mater. Sci. Tech. 1990;6:1157–66. https://doi.org/10.1179/mst.1990.6.11.1157.

[55] Cavazos JL. Characterization precipitates formed in a ferritic stainless steel stabilized with Zr and Ti additions. Mater. Charact. 2006;52:96–101. https://doi.org/10.1016/j.matchar.2005.05.006.

[56] Hall EO, Algie SH. The sigma phase. Metall Rev 1966;11:61–88. https://doi.org/10.1179/mtlr.1966.11.1.61.

[57] Premachandra K, Cartie MB, Eric RH. Effect of stabilising elements on formation of σ phase in experimental ferritic stainless steels containing 39%Cr. J Mater Sci Technol 1992;8:437–42. https://doi.org/10.1179/mst.1992.8.5.437.

[58] Vasilyuk PM, Butenko LI. Improving the oxidation resistance of Fe-Cr alloys. Russ. Metal. 1989;1:157–60.

[59] Boulanger L, Bisson A, Tavassoli AA. Labyrinth structure and persistent slip bands in fatigued 316 stainless steel. Phil Mag A 1985;51:L5–Lll. https://doi.org/10.1080/01418610.1985.12069154.

[60] Tjong SC. Transmission electron microscope observations of the dislocation substructures induced by cyclic deformation of the ferritic Fe-25Cr-(2-4)Al and Fe-19Cr-4Ni-2Al alloys. Mater. Charact. 1991;26:109–21. https://doi.org/10.1016/1044-5803(91)90071-B.

[61] Mughrabi H, Ackerman F, Herz K. Persistent slip bands in fatigued face-centered and body centered cubic metals. In: Fong JT, editor. Fatigue mechanisms. Philadelphia: American Society for Testing and Materials; 1979. p. 69–105.

[62] Li Z, Yang Y, Qi Y. Effect of Mn contents on σ precipitation and mechanical properties of ultra-low nickel 22-23% Cr duplex stainless steel aged at 850 ∘C. Mater Today Commun 2024;38:108274. https://doi.org/10.1016/j.mtcomm.2024.108274.

[63] Zhang S, Li H, Jiang Z, Li Z, Wu J, Zhang B, Duan F, Feng H, Zhu H. Influence of N on precipitation behavior, associated corrosion and mechanical properties of super austenitic stainless steel S32654. J Mater Sci Technol 2020;42:143–55. https://doi.org/10.1016/j.jmst.2019.10.011.

[64] EN 10088-1: European standard norme européenne europäische norm: stainless steels- Part 1: list of stainless steels. 2014.

[65] Yi Y, Cho P, Al Zaabi A, Addad Y, Jang C. Potentiodynamic Polarization behavior of AISI type 316 stainless steel in NaCl solution. Corros. Sci 2013;74:92–7. https://doi.org/10.1016/j.corsci.2013.04.028.

[66] Pradhan SK, Bhuyan P, Mandal S. Influence of the individual microstructural features on pitting corrosion in type 304 austenitic steel. Corros. Sci 2019;158: 108091. https://doi.org/10.1016/j.corsci.2019.108091.

[67] Santamaria M, Tranchida G, Di Franco F. Corrosion resistance of passive films on different stainless-steel grades in food and beverage industry. Corros. Sci 2020; 173:108778. https://doi.org/10.1016/j.corsci.2020.108778.

[68] West JM. Basic corrosion and oxidation. second ed. New York: Ellis Horwood; 1986.

[69] Cavazoz JL. Characterization precipitates formed in a ferritic stainless steel stabilized with Zr and Ti additions. Mater. Charact. 2006;52:96–101. https://doi.org/10.1016/j.matchar.2005.05.006.

[70] Liu X, Shan D, Song Y, En-Hou Han. Influence of yttrium element on the corrosion behaviors of Mg-Y binary magnesium alloy. J. Magnes. Alloy. 2017;5:26–34. https://doi.org/10.1016/j.jma.2016.12.002.

[71] Sudholz AD, Gusieva K, Chen XB, Muddle BC, Gibson MA, Birbilis N. Eletrochemical behaviour and corrosion of Mg-Y alloys. Corros. Sci. 2011;53:2277–82. https://doi.org/10.1016/j.corsci.2011.03.010.

[72] Wang X, Gao Y, Li Y. Effect of yttrium on the corrosion behavior of 09CrCuSb alloy in NaCl solution. Corros. Sci. 2014;87:211–7. https://doi.org/10.1016/j.corsci.2014.06.030.

[73] Ali-Löytty H, Hannula M, Honkanen Mari, Östmam K, Lahtonen K, Valden M. Grain orientation dependent Nb-Ti microalloying mediated surface segregation on ferritic stainless steel. Corros. Sci. 2016;112:204–13. https://doi.org/10.1016/j.corsci.2016.07.024.

[74] Park KH, Hwang Moon-Jin, Song Ho-Jun, Park Yeong-Joon. Electrochemical and mechanical properties of cast Ti-V alloys for dental applications. Int J Electrochem Sci 2016;11:5552–63. https://doi.org/10.20964/2016.07.64.

[75] Yanh G, Du Y, Chen S, Ren Y, Ma Y. Effect of secondary passivation on corrosion behavior and semiconducting properties of passive film of 2205 duplex stainless steel. J Mater Res Technol 2021;15:6828–40. https://doi.org/10.1016/j.jmst.2021.11.118.

[76] Mou L, Bian T, Zhang S, Liu B, et al. New sights on intergranular corrosion resistance mechanism of type 304 austenitic stainless stell by adjusting carbon contents. J Mater Res Technol 2023;26:666–80. https://doi.org/10.1016/j.jmst.2023.07.220.

[77] Trompette JL, Massot L. Kin Chronoamperometric study of the passive behaviour of tantalum in hostile media during water addition. Corros. Sci. 2012;57:175–81. https://doi.org/10.1016/j.corsci.2011.12.020.

[78] Orazem ME, Pébère N, Tribollet B. Enhanced graphical representation of electrochemical impedance data. J. Electrochem. Sci. 2006;153:B129–36. https://doi.org/10.1149/1.2168377.

[79] Gharbi O, Tran Mai TT, Tribollet B, Turmine M, Vivier V. Revisting cyclic voltammetry and electrochemical impedance spectroscopy analysis for capacitance measurements. Electrochim Acta 2020;343:136109. https://doi.org/10.1016/j.electacta.2020.136109.

[80] Gao X, Xia C, Zhang X, Jing Q, Ma M, Qin J, Liu R. Effects of iron content on the microstructure and corrosion behavior of Ti-30Zr-5Al-3VxFe alloys. Mater Chem Phys 2018;218:87–97. https://doi.org/10.1016/j.matchemphys.2018.07.033.

[81] Hirschorn B, Orazem ME, Tribollet B, Vivier V, Frateur I, Musiani M. Determination of effective capacitance and film thickness from constant-phase-element parameters. Electrochim Acta 2010;55:6218–27. https://doi:10.1016/j.electacta.2009.10.065.

[82] Orazem ME, Tribollet B. Electrochemical impedance spectroscopy. http://doi.org/10.1002/9780470381588; 2008.

[83] Brug GJ, G Van Den Eeden AL, Sluyters-Rehbach M, Sluyters JH. The analysis of electrode impedances complicated by the presence of a constant phase element. J Electroanal Chem 1984;176:275–95. https://doi.org/10.1016/S0022-0728(84)80324-1.

[84] Barcia OE, Mattos OR. The role of chloride and sulphate anions in the iron dissolution mechanism studied by impedance measurements. Electrochim Acta 1990;35:1003–9. https://doi.org/10.1016/0013-4686(90)90035-X.

[85] Keddam M, Mattos OR, Takenouti H. Mechanism of anodic dissolution of iron-chromium alloys investigated by electrode impedances - I. Experimental results and reaction model. Electrochim Acta 1986;31:1147–58. https://doi.org/10.1016/0013-4686(86)80127-X.

[86] Keddam M, Mattos OR, Takenouti H. Mechanism of anodic dissolution of iron-chromium alloys investigated by electrode impedances-II. Elaboration of the reaction model. Electrochim Acta 1986;31:1159–65. https://doi.org/10.1016/0013-4686(86)80128-1.

[87] Wang Y, Yu H, Wang L, Li M, Si R, Sun D. Research on the structure-activity relationship of Fe-Cr alloy in marine environment based on synchrotron radiation: effect of Cr content. Surf. Interfaces 2021;26:101370. https://doi.org/10.1016/j.surfin.2021.101370.

[88] Guo Q, Liu J, Yu M, Li S. Effect of passive film on mechanical properties of martensitic stainless steel 15-5PH in a neutral NaCl solution. Appl Surf Sci 2015;327:313–20. https://doi.org/10.1016/j.apsusc.2014.11.154.

[89] Refait P, Jeannin M, Urios T, Fagot A, Sabot R. Corrosion of low alloy steel in stagnant artificial or stirred natural seawater: the role of Al and Cr, Mater. Corrosion 2019;70:985–95. https://doi.org/10.1002/maco.201810753.

[90] Xu L, Wang B, Zhu J, Li W, Zheng Z. Effect of Cr content on the corrosion performance of low-Cr alloy steel in a CO_2 environment. Appl Surf Sci 2016;379:39–46. https://doi.org/10.1016/j.apsusc.2016.04.049.

[91] Ramya S, Krishna DNG, Mudali UK. In-situ Raman and X-ray photoelectron spectroscopic studies on the pitting corrosion of modified 9Cr-1Mo steel in neutral chloride solution. Appl Surf Sci 2018;428:1106–18. https://doi.org/10.1016/j.apsusc.2017.09.179.

[92] Wang Z, Zhang L, Tang X, Zhang Z, Lu M. The surface characterization and passive behavior of Type 316L stainless steel in H_2S-containing conditions. Appl Surf Sci 2017;423:457–64. https://doi.org/10.1016/j.apsusc.2017.06.214.

[93] Li W, Xu L, Qiao L, Li J. Effect of free Cr content on corrosion behavior of 3Cr steels in a CO_2 environment. Appl Surf Sci 2017;425:32–45. https://doi.org/10.1016/j.apsusc.2017.06.320.

[94] Jiang Z, Dai X, Middleton H. Effect of silicon on corrosion resistance of Ti–Si alloys. Mater Sci Eng B 2011;176:79–86. https://doi.org/10.1016/j.mseb.2010.09.006.

[95] Macdonald DD, Biaggio SR, Song H. Steady-state passive films, interfacial kinetic effects and diagnostic criteria. J Electrochem Soc 1992;139:170–7. https://doi.org/10.1149/1.2069165.

[96] Macdonald DD. Passivity – the key to our metals-based civilization. Pure Appl Chem 1999;71:951–78. https://doi.org/10.1351/pac199971060951.

[97] Atkinson A, Levy MR, Roche S, Rudkin RA. Defect properties of Ti-doped Cr_2O_3. Solid State Ion 2006;177:1767–70. https://doi.org/10.1016/j.ssi.2005.11.015.

[98] Blacklocks AN, Atkinson A, Packer RJ, Savin SLP, Chadwick AV. An XAS study of the defect structure of Ti-doped α-Cr_2O_3. Solid State Ion 2006;177:2939–44. https://doi.org/10.1016/j.ssi.2006.08.028.

[99] Yao J, Macdonald DD, Dong C. Passive film on 2205 duplex stainless steel studied by photo-electrochemistry and ARXPS methods. Corrosion Sci 2019;146:221–32. https://doi.org/10.1016/j.corsci.2018.10.020.

[100] Hagel WC, Seybolt AU. Cation diffusion in Cr_2O_3. J Electrochem Soc 1961;108:1146–52. https://doi.org/10.1149/1.2427973.